Bull Volcanol (2016) 78: 32
DOI 10.1007/s00445-016-1020-9

RESEARCH ARTICLE

The ~AD 1250 effusive eruption of El Metate shield volcano (Michoacán, Mexico): magma source, crustal storage, eruptive dynamics, and lava rheology

Magdalena Oryaëlle Chevrel[1] · **Marie-Noëlle Guilbaud**[1] · **Claus Siebe**[1]

Received: 13 September 2015 / Accepted: 28 February 2016 / Published online: 28 March 2016

Abstract Medium-sized volcanoes, also known as *Mexican shields* due to their andesitic composition and slightly higher slope angles in comparison to Icelandic shields, occur across the Trans-Mexican Volcanic Belt and represent nearly one third of all volcanic edifices in the Michoacán-Guanajuato Volcanic Field (MGVF). Many questions about their origin and eruptive dynamics remain unanswered. Here, we focus on El Metate, the youngest (~AD 1250) monogenetic shield volcano of the MGVF and the most voluminous (~9.2 km^3 dense rock equivalent) Holocene eruption in Mexico. Its eruptive history was reconstructed through detailed mapping, geochemical analysis (major and trace elements, Sr-Nd-Pb isotopic data), and rheological study of its thick andesitic flows. Early and late flow units have distinct morphologies, chemical and mineralogical compositions, and isotopic signatures which show that these lavas were fed by two separate magma batches that originated from a heterogeneous mantle source and followed distinct differentiation paths during their ascent. Thermobarometry calculations constraining the conditions of crystallization indicate a temporary storage of the last erupted magma batch at a depth of ~7–10 km. Lava rheology was estimated using petrographic characteristics, geochemical data, and flow dimensions. The magma viscosity increased from 10^2–10^3 Pa s prior to eruption through 10^6–10^8 Pa s during ascent, to 10^9–10^{11} Pa s during lava emplacement. Though magma viscosity was quite high, the eruption was purely effusive. The explosive eruption of such a large magma volume was probably avoided due to efficient open system degassing (outgassing) of the magma as it ascended through the uppermost crust and erupted at the surface.

Keywords Mexican shield · Andesite · Monogenetic · Blocky flow · Lava rheology · Holocene

Editorial responsibility: P. Wallace

Electronic supplementary material The online version of this article (doi:10.1007/s00445-016-1020-9) contains supplementary material, which is available to authorized users.

✉ Magdalena Oryaëlle Chevrel
oryaelle.chevrel@gmail.com

[1] Departamento de Vulcanología, Instituto de Geofísica, Universidad Nacional Autónoma de México, Coyoacán, Mexico D.F., Mexico

Introduction

Small- to medium-sized shield volcanoes are an important component of many volcanic fields on Earth (e.g., Idaho, USA, Greeley 1982; Hawaii, USA, Decker et al. 1987; Michoacán, Mexico, Hasenaka 1994; Iceland, Rossi 1996; the Cascades, USA, Hildreth 2007) and other planets (e.g., Moon, Guest and Murray 1976; Venus, Guest et al. 1992; Mars, Baptista et al. 2008). The Trans-Mexican Volcanic Belt (TMVB), one of the most complex and active continental arcs worldwide, displays a large number of such medium-sized volcanoes. In particular, they represent nearly one third of the ~1500 edifices of the ~40,000-km^2 Michoacán-Guanajuato Volcanic Field (MGVF, Fig. 1), which is not only the largest monogenetic field in the TMVB (Hasenaka and Carmichael 1985a) but also of the entire Earth (Valentine and Connor 2015). Although the exact causes responsible for the great number of monogenetic volcanoes in the MGVF (which also happens to be the region where the TMVB reaches its greatest width) are still poorly understood, their high frequency of occurrence may be related to the unique geometric configuration of the subduction zone (Pardo and Suárez 1995; Gómez-Tuena et al. 2007; Johnson

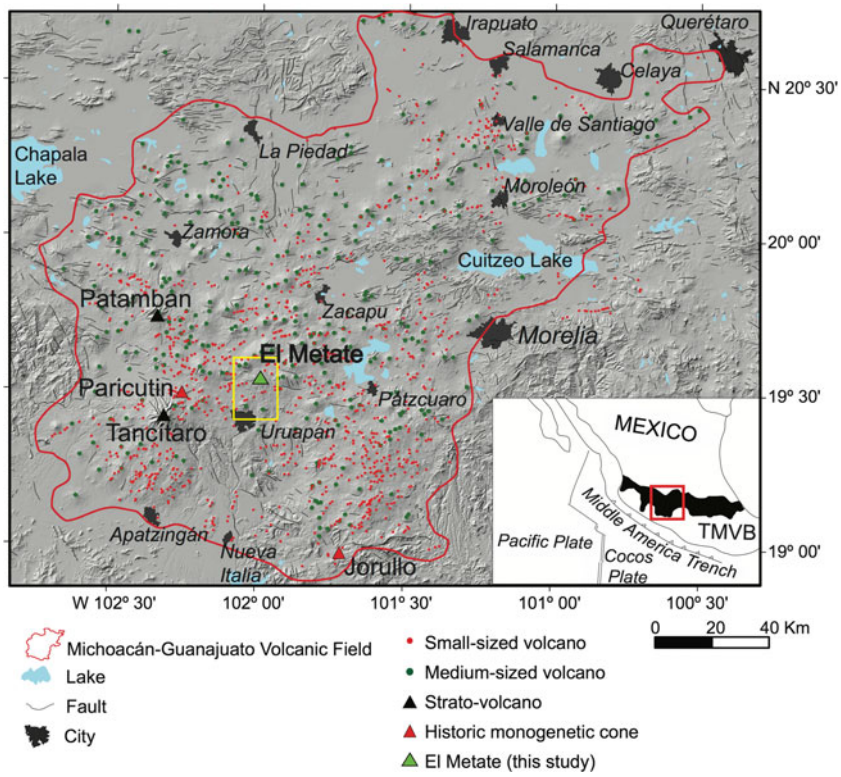

Fig. 1 Digital elevation model of the Michoacán-Guanajuato Volcanic Field (MGVF, outlined in *red*) showing the location of El Metate shield volcano. *Yellow rectangle* indicates the study area shown in detail in Fig. 2. Small-sized and medium-sized volcano database modified after Hasenaka (2009, personal communication). *Inset map* at the *lower right corner* shows the location of the MGVF within the Trans-Mexican Volcanic Belt (TMVB)

et al. 2009; Blatter and Hammersley 2010; Kim et al. 2012) that controls the location and size of magma generation areas and the magnitude of crustal extension. We speculate that the large number of monogenetic volcanoes over such a wide area might be related to the near-horizontal position at a depth of 90–120 km of this segment of the subducting oceanic Cocos plate underneath the continental North America Plate (Kim et al. 2012). Such a low subduction angle at depth might be inducing partial hydrous melting of the mantle wedge over a wide area underneath a ~40-km-thick continental crust, instead of favoring the more common case in which magmas are generated and repeatedly rise along a much narrower zone leading to the formation of a chain of stratovolcanoes.

The origin of the magmas, the eruption dynamics, and the distribution of volcanic edifices (especially of scoria cones) in the MGVF have been the focus of many previous studies (e.g., Williams 1950; Fries 1953; Hasenaka and Carmichael 1985a, b, 1987; Connor 1987, 1990; Hasenaka et al. 1994; Ownby et al. 2007, 2011; Gómez-Tuena et al. 2007; Johnson et al. 2009; Guilbaud et al. 2009, 2011, 2012; Pola et al. 2014; Siebe et al. 2014), yet there are relatively few studies focusing on the medium-sized volcanoes (Hasenaka and Carmichael 1986; Roggensack 1992; Ban et al. 1992; Hasenaka et al. 1994; Hasenaka 1994). The volumes of the MGVF shield volcanoes vary between 0.5 and 10 km^3 and are considerably larger than those of typical scoria cones (average of 0.021 km^3) but smaller than those of the two stratovolcanoes (Tancítaro and Patamban) in this field (~50 km^3, Hasenaka 1994). These medium-sized volcanoes have generally slightly steeper slopes (5–15°) than Icelandic shields (Hasenaka 1994; Roggensack 1992; Whitford-Stark 1975) and distinctly more evolved compositions (basaltic-andesitic to andesitic), which led to their designation as *Mexican shield*s (Hasenaka 1994). Although outnumbered by smaller volcanoes (mostly scoria cones), they nevertheless represent nearly 70 % of the total volume erupted since 1 Ma (Hasenaka 1994) and hence played a considerable role in the formation of the MGVF. However, the source, storage, and transport as well as the physical properties (density, viscosity, volatile content, etc.) of the magma involved in these eruptions remain poorly constrained.

In this paper, we provide new insights on magmatic processes during the ~AD 1250 eruption of El Metate, which is both the most recent monogenetic shield in Mexico and the largest andesitic effusive eruption during the Holocene worldwide (Chevrel et al. 2016). The only previous geochemical study of El Metate lavas (Losantos et al. 2014) did not specify sampling locations and reported only major element data. Here, we first summarize the main results of a recent study focused on the age, volume, chronology, and impact of the eruption (Chevrel et al. 2016) and then present new data on lava morphology. Next, we describe in detail the geochemistry (major, trace elements, and Sr-Nd-Pb isotopic data) and petrology of the distinct lava units and use this information to constrain the magma source, storage conditions, and lava rheology and to propose an eruptive model.

Age, volume, and chronology of lava flow emplacement

El Metate volcano (N 19° 32′ 19″; W 101° 59′ 34″, 2910 m asl, Fig. 1) erupted a volume of 9.2 km^3 (dense rock equivalent) of andesitic lava (Chevrel et al. 2016). Detailed fieldwork shows that the eruption was purely effusive since neither ash nor spatter deposits from El Metate were found in its vicinity (Chevrel et al. 2016). If El Metate had initiated with a Strombolian phase (with ash deposits now mostly buried below the thick lava flows), the old edifice that crops out ~1.5 km south of El Metate's summit (Fig. 2) should be covered by several meters of fresh coarse ash. However, we only found a 70-cm-thick strongly altered scoriaceous ash fallout (dated at 13,480 ± 50 years BP that predates significantly El Metate's eruption) under a well-developed clayey soil.

In addition, paleosols are absent between the different flow units. The latter also display similarly well-preserved surface morphologies, indicating that the entire edifice was formed during one single eruptive event. The eruption took place ~AD 1250, and since it is absent from colonial chronicles, it must have ended well before the invasion of the Spaniards that occurred only 275 years later in the 1520s. Because of the large area covered by the lava flows (103 km^2) and the concomitant disruption of the regional hydrological network, local human populations might have been forced to migrate to the neighboring lacustrine basins (Zacapu and Pátzcuaro) in the east contributing to the social processes that led to the rise of the Tarascan empire that initiated around that time (Chevrel et al. 2016).

The morphology of El Metate is remarkably well preserved and exposed (Fig. 3). The volcano is composed of a central dome (1 km wide, 300 m high) from which several voluminous lava flows that form distinct units radiate (Fig. 2). Lava flows directed to the south reached longer distances (<15 km) than flows emitted to the N, due to different topographical

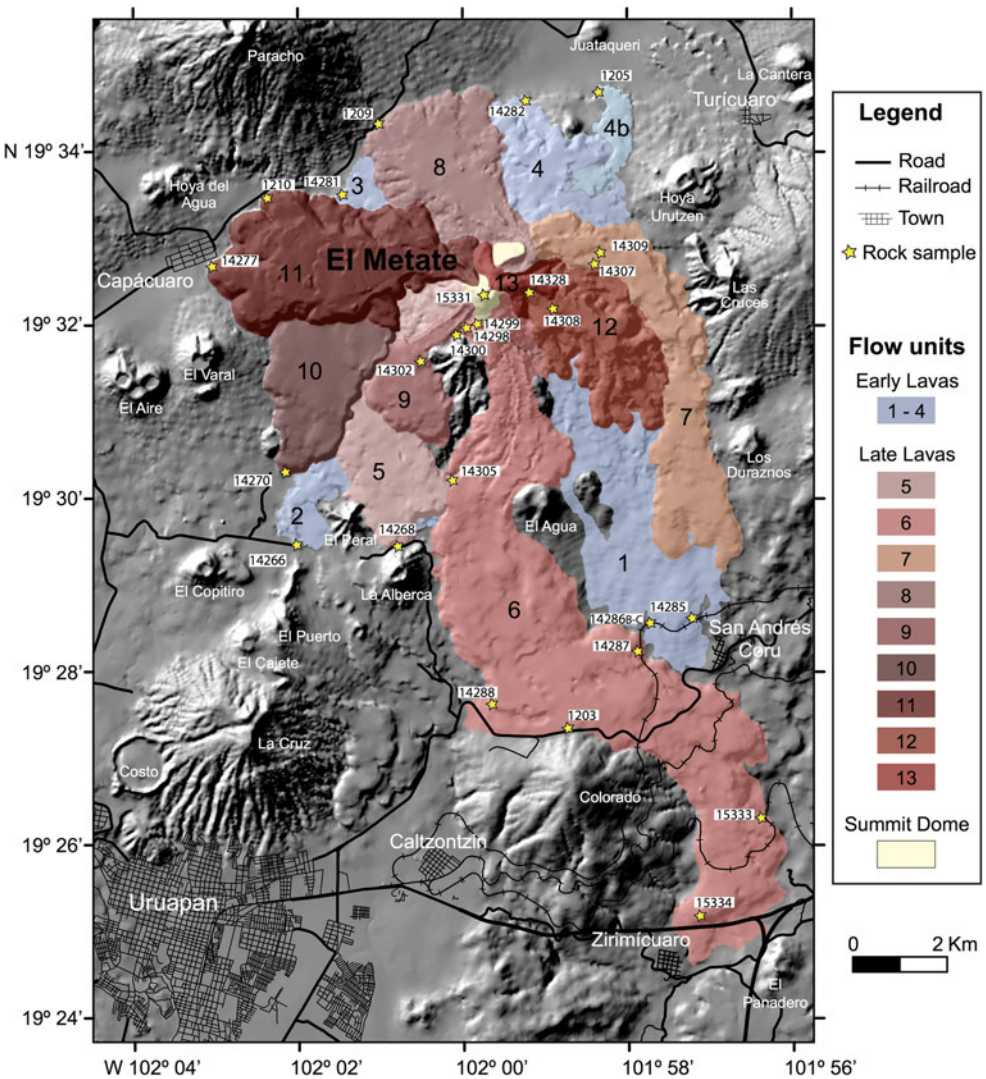

Fig. 2 Digital elevation model of El Metate shield volcano showing emplacement sequence (*1–13*) of the different lava flows and surrounding volcanoes. Sampling locations of analyzed rocks are indicated

gradients and the presence of the older prominent Paracho shield to the N. For this reason, the ~10-km wide and ~600-m high shield is slightly asymmetric. Thirteen flow units were identified from their stratigraphic relations (Fig. 2). Lava flow units F1 to F4 are clearly below lava units F5 to F13, and thus, these form the early and late lava groups, respectively. The lateral contacts of early lava units are however not exposed; thus, their relative time of emplacement is not known. The proposed numeration from F1 to F4 is hence tentative, except for F4b, which issued from unit F4 and thus must be younger than F4. By contrast, the relative time of emplacement of late lavas can be much better constrained due to clear contacts between the flows (Fig. 2) and sharp compositional differences between stratigraphically lower F5 to F8 units and stratigraphically higher F9 to F13 units. Nevertheless, the relative order between flow units F6 and F7 is only partly known and their composition is similar (see below); hence, their numeration is also tentative (these uncertainties do not affect our final eruptive model, see below).

Lava flow morphology

The early and late lavas are morphologically distinct. The fronts of the early flows average <40 m thick and their surface texture ranges from rubbly-'a'ā to blocky in contrast to late flows that have thick (<150 m) fronts and blocky surfaces (terms used as defined in Kilburn 2000). In comparison with early lavas whose proximal surfaces are not exposed, most of the late flows can be traced from source to front where some flows split into multiple lobes. These flows have well-defined open channels separated from wide flat-topped margins (*levées*) by a clear shear zone that is continuous from source to front (Fig. 4). The channels are typically narrow near the source and broaden downslope, as the topographic gradient decreases, forming fan-shaped or straight flows depending, respectively, on whether they flowed on a near flat or more inclined topography (Fig. 4). The lava surfaces inside the channels display thick and widely spaced cross-flow ridges (*ogives*).

The morphological features observable at El Metate are typical for highly viscous silicic *coulées*, e.g., the Chao dacitic flow (de Silva et al. 1994), the coulées at San Pietro Island (Cioni and Funedda 2005), or the rhyolitic obsidian flow of Cordón Caulle (Tuffen et al. 2013). Nevertheless, it is worth mentioning that the size of the El Metate lava flows is exceptionally large. The longest (F6) is on average 15 km long, <4 km wide, and ~70 m thick, corresponding to a volume of 2.2 km^3, and the thickest (F11) is on average 5 km long, ~2 km wide, and 150 m thick, corresponding to a volume of 1.8 km^3. These flows are among the most voluminous single lava lobes so far reported (Wadge and Lopes 1991). Flows of similarly large sizes are usually more silicic [1–3 km^3 San Pedro andesitic flow, Chile (Francis et al. 1974); 4.4 km^3 Payun Matru trachytic flow, Argentina (González Díaz 1972); 2.1 km^3 Copales dacitic lava flow from Ceburoco, Mexico (Sieron and Siebe 2008); 1–2 km^3 dacitic to rhyolitic Big Glass Mountain, USA (Eichelberger 1975); 24 km^3 Chao dacitic flow, Chile (Guest and Sanchez 1969)]. Thus, El Metate produced some of the most voluminous andesitic flows that have been reported, and their young age has made it possible to study them in detail.

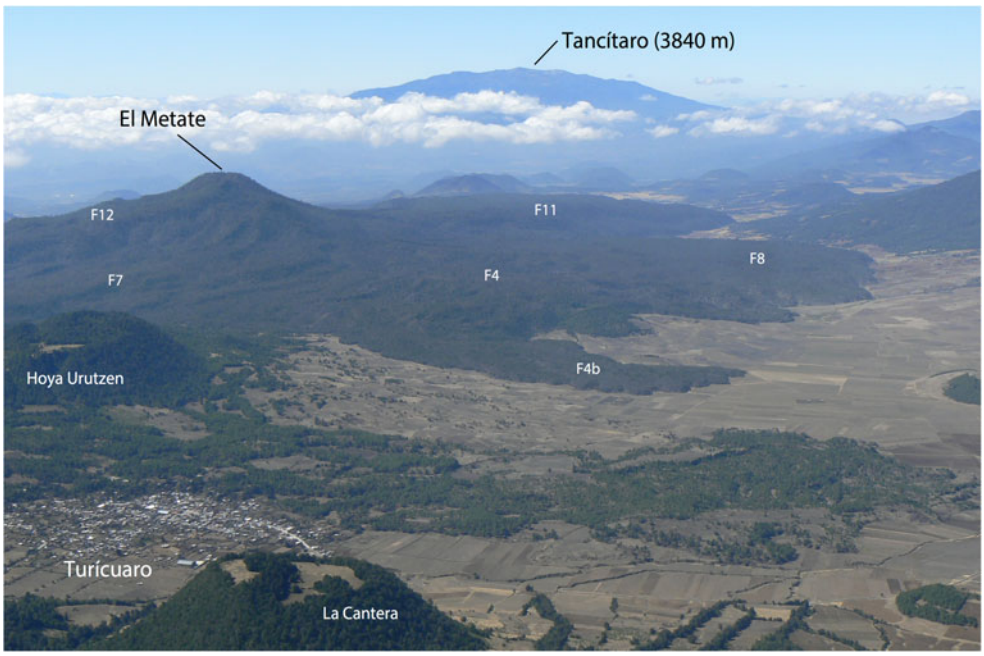

Fig. 3 Aerial view of El Metate (2910 m asl) from the east with the stratovolcano Tancítaro in the background and the village of Turícuaro in the foreground. Different El Metate lava flow units (F4, F4b, F7, F8, F11, and F12) are indicated. Photo taken February 7, 2010

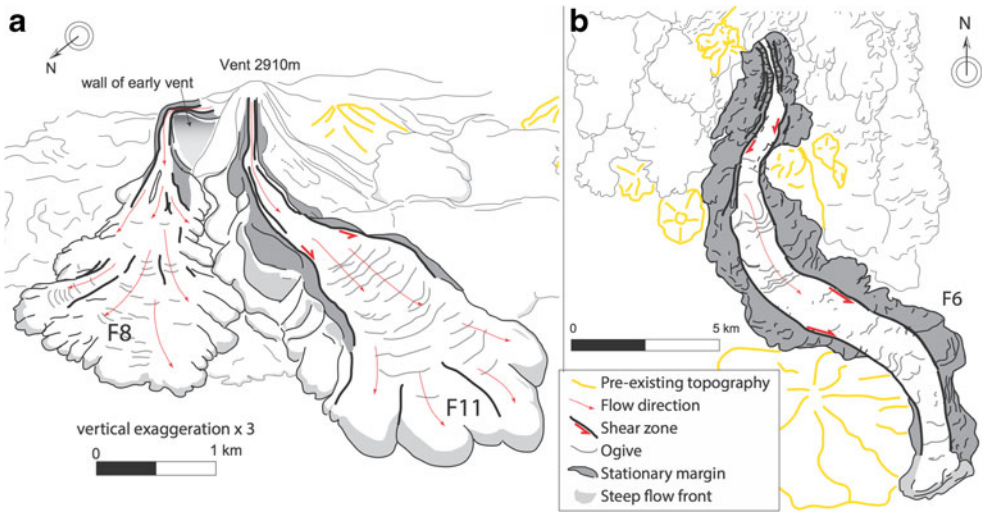

Fig. 4 Schematic representation of major lava flow features. **a** Oblique view from the NW of the fan-shaped flows F8 and F11. **b** Vertical view of the straight channel flow F6

Sampling and analytical methods

Rock samples were collected from the interiors of surface blocks, to avoid alteration. We first sampled the flow fronts that were of easy access and then collected rock samples during long hikes along the flow margins or across their interiors where possible (Fig. 2). Twenty-seven whole rock samples from El Metate were analyzed for major and trace elements at Activation Laboratories Inc., Ancaster, Canada (analytical methods, including detection limits and analytical uncertainties, are reported in Table 1). Thin sections from each lava unit were studied under a polarizing microscope. Modal mineralogical analyses were carried out with the aid of an automated stage. Mineral compositions were determined using a JEOL JXA-8900R electron microprobe at the Laboratorio Universitario de Petrología (LUP), Instituto de Geofísica, UNAM, Mexico City. The measuring conditions were set at an accelerating voltage of 20 kV and a beam current of 20 nA (with a diameter of 1 μm), and counting times were 40 s for all elements. Elements were calibrated from an assortment of mineral standards taken from SPI supplies® reference standards for X-ray analysis (SPI# 2757-AB). Sr-Nd-Pb-isotope ratios were determined for six samples representative of the distinct lava groups at the Laboratorio Universitario de Geoquímica Isotópica (LUGIS), Instituto de Geofísica, UNAM. Sr-Nd isotope ratios were determined with a Thermo Scientific Triton Plus thermal-ionization mass spectrometer (TIMS) equipped with nine Faraday cups, and Pb isotopes were determined with a Finnigan MAT 262 TIMS equipped with eight Faraday cups. All the measurements were done in static mode. Further details of the analytical procedures can be found in Table 2 and in Schaaf et al. (2005).

Results

Mineralogy and petrography

Volume percent of the different phases present in the samples (crystals, groundmass, vesicles) and average mineral and glass compositions are reported in Tables 3 and 4, respectively. All lavas contain plagioclase as phenocrysts (0.7–16.9 vol%) and microphenocrysts (12.5–30.8 vol%) and augite and hypersthene often as phenocrysts (<3 vol%) and as microphenocrysts (0.2–13.5 vol%) embedded in a light-brown groundmass consisting of microlites of the same mineral phases plus oxides and minor interstitial glass (Table 3). In addition, the early lavas F1 and F4b contain 2.4–6.6 vol% olivine phenocrysts, in contrast to all late lava units (F5 to F13 and dome) that contain 1.2–6.3 vol% hornblende phenocrysts and lack olivine. The other early lavas (F2, F3, and F4) do not contain olivine or hornblende. Vesicles represent <9 vol% of the lavas, except in rocks from the summit dome area and from late-stage proximal lavas (F11 to F13) that contain 11 to 29 vol% vesicles.

Olivine phenocrysts are up to 1 mm long, euhedral to subhedral, and show resorption textures with reaction rims of pyroxene (Fig. 5a, b). Pyroxene phenocrysts are <0.5 mm, they occasionally show disequilibrium textures, and the microphenocrysts are often found as clusters. Hypersthene microphenocrysts are elongated and have oxide inclusions. Plagioclase phenocrysts are tabular, <0.5 mm long, and frequently oscillatory-zoned and commonly contain inclusions of glass, apatite, pyroxene, and rarely opaques, which were not observed inside the acicular microphenocrysts and microlites. Hornblendes are <1 cm long and show variable morphology. Some are pristine and others present disequilibrium textures. Some of the crystals have a rim made of a

Table 1 Whole rock major (in wt%) and trace element (in ppm) analyses of rock samples from El Metate lavas

Sample no.			14300	14286-C	14285	14305	14286	14307	14287	14268	14288	1203
Flow unit			F5 ?	F1	F1	F6	F1	F7	F6	F5	F6	F6
Latitude (N)			19° 31′ 50″	19° 28′ 27.3"	19° 28′ 28.0″	19° 30′ 13.5″	19° 28′ 28.60″	19° 32′ 44.9″	19° 28′ 09.7″	19° 29′ 21.6″	19° 32′ 13.3″	19° 27′ 16.3″
Longitude (W)			101° 59′ 55.6″	101° 57′ 40.4″	101° 57′ 06.0″	102° 00′ 06.4″	101° 57′ 7.59″	101° 58′ 10.3″	101° 57′ 46.9″	102° 00′ 49.8″	102° 06′ 24.4″	101° 58′ 35.8″
Altitude asl (m)			2550	1790	1797	2127	2321	2494	1777	2064	1868	1860
wt%	An. met.	Det. limits										
SiO_2	FUS-ICP	0.01	54.93	56.52	57.38	57.42	57.45	57.63	57.99	58.23	58.34	58.38
Al_2O_3	FUS-ICP	0.01	17.37	17.16	17.29	18.23	17.06	17.76	18.33	17.89	18.34	17.85
Fe_2O_3 (T)	FUS-ICP	0.01	5.9	7.22	7.19	5.95	7.34	6	5.79	5.81	5.86	5.78
MnO	FUS-ICP	0.01	0.095	0.12	0.12	0.097	0.12	0.10	0.09	0.09	0.10	0.096
MgO	FUS-ICP	0.01	4.2	5.07	5.19	3.62	5.1	3.18	3.12	3.18	3.09	3.1
CaO	FUS-ICP	0.01	8.38	7.05	7.19	7.82	7	7.17	7.19	7.55	7.3	7.11
Na_2O	FUS-ICP	0.01	3.9	3.83	3.86	4.04	3.8	3.95	4.1	3.95	4.11	3.98
K_2O	FUS-ICP	0.01	1.54	1.41	1.4	1.23	1.42	1.73	1.19	1.51	1.24	1.3
TiO_2	FUS-ICP	0.01	0.744	0.89	0.90	0.756	0.90	0.79	0.69	0.74	0.71	0.707
P_2O_5	FUS-ICP	0.01	0.3	0.24	0.24	0.23	0.24	0.33	0.23	0.28	0.22	0.24
LOI		0.01	2.5	0.21	−0.07	1.01	0.52	0.77	0.22	0.42	0.1	0.19
Total			97.4	99.5	100.8	99.4	100.4	98.6	98.7	99.2	99.3	98.5
S	TD-ICP	0.001	0.008	0.025	0.03	0.005	0.026	0.046	0.002	0.034	0.045	0.034
Sc	INAA	0.01	13	17.9	18.1	13.5	17.8	13.9	12.6	13.4	13.6	13
V	FUS-ICP	5	126	149	153	128	149	128	118	125	118	121
Cr	INAA	0.5	43.4	141	131	50	146	45.1	49.8	49.2	36	29.6
Co	INAA	0.1	16.2	25.9	24.7	18.4	26.1	22.2	17.6	16.4	16.6	15.4
Ni	TD-ICP	1	25	87	88	23	84	25	21	24	22	23
Cu	TD-ICP	1	24	34	37	23	30	27	16	32	29	26
Zn	MI/TD-ICP	1	65	62	64	64	62	71	68	65	67	69
Ga	FUS-MS	1	22	18	18	23	18	21	23	22	21	20
Ge	FUS-MS	0.5	1.2	2.4	1.9	1.2	1.7	1.7	1.4	1.2	1.7	2.4
Br	INAA	0.5	<0.5	2.2	<0.5	<0.5	<0.5	<0.5	<0.5	<0.5	<0.5	2.1
Rb	FUS-MS	1	27	22	21	18	22	28	17	24	16	18
Sr	FUS-ICP	2	1478	502	502	1561	504	1581	1384	1579	1493	1530
Y	FUS-ICP	1	12	18	17	12	19	12	11	12	11	11
Zr	FUS-ICP	1	130	138	142	114	149	157	100	131	111	123
Nb	FUS-MS	0.2	3.3	6.1	6.4	3.7	7.1	1.5	3	3.9	1.2	4.1
Sn	FUS-MS	1	<1	2	2	<1	<1	<1	<1	<1	<1	1
Sb	INAA	0.1	<0.1	<0.1	<0.1	<0.1	<0.1	1	<0.1	<0.1	0.8	<0.1
Cs	FUS-MS	0.1	0.6	0.5	0.5	0.4	0.5	0.7	0.3	0.5	0.3	0.5
Ba	FUS-ICP	1	472	478	483	377	476	504	384	450	377	370
La	FUS-MS	0.05	24.7	17.9	17.1	21.4	19	24.6	18	23.2	18.3	20.5
Ce	FUS-MS	0.05	53.1	35.3	34.6	46.2	37.7	52.9	39.1	49.3	39	45
Pr	FUS-MS	0.01	6.84	4.58	4.46	5.83	4.87	6.97	4.91	6.58	5.05	5.37
Nd	FUS-MS	0.05	26	18.4	17.8	22.2	19.8	27.6	18.9	26.2	19.8	21.4
Sm	FUS-MS	0.01	4.56	4.04	3.88	3.94	4.25	4.89	3.37	4.48	3.57	3.55
Eu	FUS-MS	0.005	1.31	1.18	1.19	1.24	1.27	1.44	1.09	1.35	1.13	1.16

Table 1 (continued)

Sample no.			14300	14286-C	14285	14305	14286	14307	14287	14268	14288	1203
Flow unit			F5 ?	F1	F1	F6	F1	F7	F6	F5	F6	F6
Latitude (N)			19° 31′ 50″	19° 28′ 27.3"	19° 28′ 28.0″	19° 30′ 13.5″	19° 28′ 28.60″	19° 32′ 44.9″	19° 28′ 09.7″	19° 29′ 21.6″	19° 32′ 13.3″	19° 27′ 16.3″
Longitude (W)			101° 59′ 55.6″	101° 57′ 40.4″	101° 57′ 06.0″	102° 00′ 06.4″	101° 57′ 7.59″	101° 58′ 10.3″	101° 57′ 46.9″	102° 00′ 49.8″	102° 06′ 24.4″	101° 58′ 35.8″
Altitude asl (m)			2550	1790	1797	2127	2321	2494	1777	2064	1868	1860
wt%	An. met.	Det. limits										
Gd	FUS-MS	0.01	3.35	3.49	3.22	2.86	3.55	3.65	2.48	3.24	2.86	3.14
Tb	FUS-MS	0.01	0.47	0.56	0.53	0.44	0.57	0.5	0.39	0.45	0.43	0.46
Dy	FUS-MS	0.01	2.52	3.15	3.28	2.48	3.44	2.44	2.18	2.31	2.13	2.39
Ho	FUS-MS	0.01	0.48	0.59	0.62	0.47	0.67	0.45	0.43	0.43	0.42	0.43
Er	FUS-MS	0.01	1.32	1.74	1.8	1.29	1.9	1.26	1.23	1.22	1.19	1.21
Tm	FUS-MS	0.005	0.183	0.277	0.284	0.195	0.294	0.173	0.18	0.177	0.173	0.176
Yb	FUS-MS	0.01	1.14	1.82	1.9	1.3	1.82	1.1	1.16	1.1	1.13	1.13
Lu	FUS-MS	0.002	0.187	0.258	0.25	0.219	0.295	0.162	0.193	0.159	0.165	0.185
Hf	FUS-MS	0.1	2.9	3	3	2.7	3.3	3.8	2.4	3.5	2.8	2.8
Ta	FUS-MS	0.01	0.07	0.52	0.53	0.06	0.51	0.2	0.03	0.2	0.2	0.31
Pb	TD-ICP	5	<5	<5	<5	<5	<5	<5	<5	<5	<5	<5
Th	FUS-MS	0.05	2.8	1.7	1.65	2.27	1.88	2.87	1.98	2.63	1.97	2.23
U	FUS-MS	0.01	1.06	0.54	0.58	0.73	0.58	1.06	0.68	0.9	0.67	0.69

Sample no.			14300	1205	14298	15334	14277	15333	1209	1210	14309	14328
Flow unit			F5 ?	F4b	F6	F6	F11	F6	F8	F11	F7	F13
Latitude (N)			19° 31′ 50″	19° 34′ 41.6″	19° 31′ 58.8″	19° 24′ 58.2″	19° 32′ 45.0″	19° 26′ 20.2″	19° 34′ 19.9″	19° 33′ 22.3″	19° 32′ 54.7″	19° 32′ 21.2″
Longitude (W)			101° 59′ 55.6″	101° 58′ 12.6″	101° 59′ 46.9″	101° 57′ 04.4″	102° 02′ 50.8″	101° 56′ 15.9″	102° 00′ 49.9″	102° 02′ 05.8″	101° 58′ 40.8″	101° 59′ 02.2″
Altitude asl (m)			2550	2298	2537	1401	2252	1471	2352	2303	2470	2740
wt%	An. met.	Det. limits										
SiO_2	FUS-ICP	0.01	54.93	58.43	58.45	58.95	59.17	59.27	59.43	59.44	59.65	59.7
Al_2O_3	FUS-ICP	0.01	17.37	17.06	17.9	18.06	17.69	17.48	18	17.5	17.66	17.64
Fe_2O_3 (T)	FUS-ICP	0.01	5.9	6.02	5.96	5.67	5.5	5.79	6.05	5.4	5.92	5.32
MnO	FUS-ICP	0.01	0.095	0.099	0.10	0.09	0.09	0.097	0.099	0.089	0.10	0.08
MgO	FUS-ICP	0.01	4.2	3.89	3.19	3.03	3.05	3.15	3.34	2.98	3.26	3.04
CaO	FUS-ICP	0.01	8.38	6.66	7.39	6.99	6.55	7.3	6.75	6.43	7.03	6.46
Na_2O	FUS-ICP	0.01	3.9	3.68	3.99	4.09	3.97	3.94	4.22	3.86	4.09	4.12
K_2O	FUS-ICP	0.01	1.54	1.67	1.37	1.28	1.44	1.33	1.77	1.41	1.77	1.36
TiO_2	FUS-ICP	0.01	0.744	0.674	0.77	0.67	0.66	0.691	0.736	0.658	0.79	0.58
P_2O_5	FUS-ICP	0.01	0.3	0.19	0.26	0.24	0.2	0.25	0.3	0.19	0.31	0.17
LOI		0.01	2.5	−0.18	0.23	0.74	−0.16	0.53	−0.13	0.07	0.34	0.71
Total			97.4	98.4	99.4	99.1	98.3	99.3	100.7	98.0	100.6	98.5
S	TD-ICP	0.001	0.008	0.037	0.029	0.002	0.027	0.002	0.032	0.026	0.042	0.002
Sc	INAA	0.01	13	14.8	13.4	12.7	13.8	13.5	13.1	12	14.6	11.9

Table 1 (continued)

Sample no.			14300	1205	14298	15334	14277	15333	1209	1210	14309	14328
Flow unit			F5 ?	F4b	F6	F6	F11	F6	F8	F11	F7	F13
Latitude (N)			19° 31′ 50″	19° 34′ 41.6″	19° 31′ 58.8″	19° 24′ 58.2″	19° 32′ 45.0″	19° 26′ 20.2″	19° 34′ 19.9″	19° 33′ 22.3″	19° 32′ 54.7″	19° 32′ 21.2″
Longitude (W)			101° 59′ 55.6″	101° 58′ 12.6″	101° 59′ 46.9″	101° 57′ 04.4″	102° 02′ 50.8″	101° 56′ 15.9″	102° 00′ 49.9″	102° 02′ 05.8″	101° 58′ 40.8″	101° 59′ 02.2″
Altitude asl (m)			2550	2298	2537	1401	2252	1471	2352	2303	2470	2740
wt%	An. met.	Det. limits										
V	FUS-ICP	5	126	135	125	118	117	123	127	117	130	114
Cr	INAA	0.5	43.4	74.1	41	34.7	46.4	45.1	41.8	30.1	46.8	42.5
Co	INAA	0.1	16.2	18	18.3	16	17.9	17.9	16.7	14.9	17	17.4
Ni	TD-ICP	1	25	48	25	22	24	22	30	25	25	25
Cu	TD-ICP	1	24	48	27	25	21	22	29	26	28	26
Zn	MI/TD-ICP	1	65	80	64	65	61	66	74	65	66	64
Ga	FUS-MS	1	22	20	21	22	21	23	19	20	21	22
Ge	FUS-MS	0.5	1.2	1.6	1.8	1.2	1.4	1.4	2.2	1.6	1.6	1.2
Br	INAA	0.5	<0.5	2.6	<0.5	<0.5	<0.5	<0.5	2.8	1.8	<0.5	<0.5
Rb	FUS-MS	1	27	28	18	19	21	19	29	20	27	19
Sr	FUS-ICP	2	1478	733	1617	1357	1155	1369	1410	1084	1587	778
Y	FUS-ICP	1	12	15	13	11	11	13	13	12	14	11
Zr	FUS-ICP	1	130	131	137	105	104	123	172	116	142	85
Nb	FUS-MS	0.2	3.3	4.3	3.8	3	3.3	3.5	4.2	4	3.9	2.2
Sn	FUS-MS	1	<1	<1	<1	3	<1	<1	1	<1	1	<1
Sb	INAA	0.1	<0.1	<0.1	<0.1	<0.1	<0.1	<0.1	0.1	<0.1	2.3	<0.1
Cs	FUS-MS	0.1	0.6	0.8	0.5	0.4	0.4	0.5	0.9	0.5	0.7	0.5
Ba	FUS-ICP	1	472	537	395	397	415	384	525	426	517	458
La	FUS-MS	0.05	24.7	18.8	23.1	17.8	16.9	18.9	23.2	17	25.8	14
Ce	FUS-MS	0.05	53.1	38.7	49	38.3	34.7	40.2	50.1	35.7	55.8	27.9
Pr	FUS-MS	0.01	6.84	4.93	6.39	4.8	4.45	5.12	5.91	4.4	7.2	3.53
Nd	FUS-MS	0.05	26	20.2	24.4	18.4	18.5	19.4	24	18	28.9	13.8
Sm	FUS-MS	0.01	4.56	4.06	4.21	3.39	3.19	3.61	4.38	3.46	5.29	2.67
Eu	FUS-MS	0.005	1.31	1.13	1.35	1.14	1.11	1.17	1.26	0.993	1.55	0.933
Gd	FUS-MS	0.01	3.35	2.78	3.02	2.49	2.65	2.66	3.52	2.3	3.44	2.22
Tb	FUS-MS	0.01	0.47	0.43	0.42	0.4	0.36	0.43	0.47	0.34	0.49	0.35
Dy	FUS-MS	0.01	2.52	2.51	2.16	2.3	2	2.37	2.27	2.03	2.44	1.92
Ho	FUS-MS	0.01	0.48	0.47	0.42	0.44	0.39	0.46	0.44	0.38	0.45	0.38
Er	FUS-MS	0.01	1.32	1.31	1.21	1.22	1.11	1.32	1.26	1.05	1.2	1.12
Tm	FUS-MS	0.005	0.183	0.195	0.184	0.176	0.162	0.192	0.186	0.155	0.175	0.155
Yb	FUS-MS	0.01	1.14	1.29	1.17	1.14	1.11	1.28	1.26	0.98	1.15	0.99
Lu	FUS-MS	0.002	0.187	0.213	0.171	0.183	0.171	0.214	0.203	0.157	0.17	0.16
Hf	FUS-MS	0.1	2.9	3	3.4	2.6	2.8	2.5	4	2.7	3.7	2
Ta	FUS-MS	0.01	0.07	0.3	0.35	0.03	0.2	0.05	0.29	0.24	0.23	<0.01
Pb	TD-ICP	5	<5	6	<5	<5	<5	<5	<5	<5	<5	<5
Th	FUS-MS	0.05	2.8	2.87	2.38	2.05	2.03	2.13	2.94	2.25	2.89	1.79
U	FUS-MS	0.01	1.06	0.92	0.85	0.7	0.66	0.7	1.01	0.71	0.99	0.63

Table 1 (continued)

Sample no.			14300	14302	14308	14270	14282	14299	14266	15331	14281
Flow unit			F5 ?	F9	F12	F10	F4	Dome	F2	Dome	F3
Latitude (N)			19° 31′ 50″	19° 31′ 29.3″	19° 32′ 15.4″	19° 30′ 18.0″	19° 34′ 33.9″	19° 32′ 7.0″	19° 29′ 24.9″	19° 32′ 19.7″	19° 33′ 29.3″
Longitude (W)			101° 59′ 55.6″	102° 00′ 14.3″	101° 58′ 44.9″	102° 01′ 56.0″	101° 59′ 01.6″	102° 39′ 40.2″	102° 01′ 55.7″	101° 59′ 34.2″	102° 01′ 22.5″
Altitude asl (m)			2550	2361	2646	2066	2314	2699	2004	2910	2298
wt%	An. met.	Det. limits									
SiO_2	FUS-ICP	0.01	54.93	59.97	60.07	60.08	60.59	60.73	60.92	61	61.37
Al_2O_3	FUS-ICP	0.01	17.37	17.71	17.61	17.68	16.7	18.15	17.09	17.61	17.17
Fe_2O_3 (T)	FUS-ICP	0.01	5.9	5.61	5.15	5.49	5.54	5.69	5.53	5.36	5.63
MnO	FUS-ICP	0.01	0.095	0.09	0.08	0.09	0.09	0.09	0.09	0.083	0.09
MgO	FUS-ICP	0.01	4.2	3.01	2.77	2.99	2.98	3.01	2.76	2.92	3.2
CaO	FUS-ICP	0.01	8.38	6.82	5.98	6.72	5.96	6.65	6.04	6.33	6.14
Na_2O	FUS-ICP	0.01	3.9	4.04	4.12	3.94	3.78	4.02	3.93	4.07	3.89
K_2O	FUS-ICP	0.01	1.54	1.47	1.51	1.46	1.71	1.45	2.09	1.45	1.9
TiO_2	FUS-ICP	0.01	0.744	0.68	0.57	0.64	0.65	0.66	0.67	0.592	0.66
P_2O_5	FUS-ICP	0.01	0.3	0.24	0.15	0.21	0.22	0.21	0.29	0.17	0.24
LOI		0.01	2.5	0.29	0.66	0.03	1.74	0.24	0.32	0.75	0.43
Total			97.4	99.6	98.0	99.3	98.2	100.7	99.4	99.6	100.3
S	TD-ICP	0.001	0.008	0.027	0.038	0.03	0.036	0.026	0.027	0.005	0.164
Sc	INAA	0.01	13	12.8	11.9	13.5	13.3	12.2	12.7	12.2	13.1
V	FUS-ICP	5	126	116	106	114	111	114	110	115	115
Cr	INAA	0.5	43.4	51.3	26.8	51	70.6	48.9	44.2	39.2	68.1
Co	INAA	0.1	16.2	15.9	18.1	16.1	18	18.5	15.3	20.5	18
Ni	TD-ICP	1	25	23	24	25	30	23	31	24	40
Cu	TD-ICP	1	24	18	27	33	27	49	29	24	15
Zn	MI/TD-ICP	1	65	62	64	67	62	62	68	63	63
Ga	FUS-MS	1	22	21	20	21	20	20	20	22	20
Ge	FUS-MS	0.5	1.2	1.9	1.8	1.7	1.1	1.9	1.5	1.3	1.9
Br	INAA	0.5	<0.5	2.5	<0.5	<0.5	4.6	4.7	<0.5	2	<0.5
Rb	FUS-MS	1	27	20	20	24	34	20	42	22	31
Sr	FUS-ICP	2	1478	1205	801	1138	672	1083	772	785	689
Y	FUS-ICP	1	12	10	9	10	14	11	16	10	16
Zr	FUS-ICP	1	130	126	82	110	140	125	166	92	165
Nb	FUS-MS	0.2	3.3	3.3	2.2	3.8	5.6	3.3	6.9	2.5	6.4
Sn	FUS-MS	1	<1	<1	2	<1	<1	2	1	<1	1
Sb	INAA	0.1	<0.1	<0.1	0.9	<0.1	0.3	<0.1	<0.1	<0.1	2.1

Table 1 (continued)

Sample no.			14300	14302	14308	14270	14282	14299	14266	15331	14281
Flow unit			F5 ?	F9	F12	F10	F4	Dome	F2	Dome	F3
Latitude (N)			19° 31′ 50″	19° 31′ 29.3″	19° 32′ 15.4″	19° 30′ 18.0″	19° 34′ 33.9″	19° 32′ 7.0″	19° 29′ 24.9″	19° 32′ 19.7″	19° 33′ 29.3″
Longitude (W)			101° 59′ 55.6″	102° 00′ 14.3″	101° 58′ 44.9″	102° 01′ 56.0″	101° 59′ 01.6″	102° 39′ 40.2″	102° 01′ 55.7″	101° 59′ 34.2″	102° 01′ 22.5″
Altitude asl (m)			2550	2361	2646	2066	2314	2699	2004	2910	2298
wt%	An. met.	Det. limits									
Cs	FUS-MS	0.1	0.6	0.5	0.6	0.6	0.8	0.5	1	0.6	0.5
Ba	FUS-ICP	1	472	433	469	436	566	436	786	467	629
La	FUS-MS	0.05	24.7	19.2	13.8	17.5	20.9	17.6	30.4	14.3	25.1
Ce	FUS-MS	0.05	53.1	39.1	27.6	35.2	41.8	36.1	59	28.5	48.6
Pr	FUS-MS	0.01	6.84	4.98	3.44	4.6	5.2	4.8	7.57	3.63	6.21
Nd	FUS-MS	0.05	26	19.8	14.1	18.4	20.1	18.3	29.1	13.8	23.7
Sm	FUS-MS	0.01	4.56	3.43	3.04	3.36	3.85	3.57	5.36	2.9	4.48
Eu	FUS-MS	0.005	1.31	1.06	0.874	1	1.16	1.07	1.47	0.899	1.34
Gd	FUS-MS	0.01	3.35	2.56	2.15	2.49	3.3	2.42	4	2.09	3.62
Tb	FUS-MS	0.01	0.47	0.38	0.32	0.37	0.54	0.37	0.58	0.34	0.55
Dy	FUS-MS	0.01	2.52	2.14	1.72	2.04	2.82	2.08	3.09	1.98	2.92
Ho	FUS-MS	0.01	0.48	0.4	0.33	0.41	0.51	0.39	0.56	0.38	0.56
Er	FUS-MS	0.01	1.32	1.2	0.88	1.16	1.47	1.08	1.57	1.07	1.66
Tm	FUS-MS	0.005	0.183	0.174	0.132	0.174	0.227	0.151	0.223	0.16	0.26
Yb	FUS-MS	0.01	1.14	1.12	0.89	1.1	1.47	0.97	1.46	1.03	1.62
Lu	FUS-MS	0.002	0.187	0.168	0.137	0.155	0.226	0.152	0.218	0.17	0.223
Hf	FUS-MS	0.1	2.9	2.9	2.3	3	3.3	3	4	2.2	3.7
Ta	FUS-MS	0.01	0.07	0.3	0.16	0.24	0.44	0.29	0.64	<0.01	0.53
Pb	TD-ICP	5	<5	<5	<5	<5	10	7	8	<5	32
Th	FUS-MS	0.05	2.8	2.22	1.9	2.14	2.81	2.02	3.26	2	3.32
U	FUS-MS	0.01	1.06	0.72	0.61	0.73	0.96	0.66	1.2	0.67	0.9

Flow unit is indicated for each sample. Note that whether sample 14300 belongs to flow unit F5 or to a younger flow unit remains unclear. Geographic coordinates are given and sampling locations are indicated in Fig. 2. Analytical uncertainties are ±100 % at the detection limits, ±15–20 % at 20 times the detection limits, and >5 % at 100 times the detection limits. Samples were pulverized with mild steel devices, which contaminate with Fe (0.1 %). MI/TD-ICP is a combination of the INAA and TD-ICP analytical methods. Further details of analytical procedures are described in the Actlabs website at www.actlabs.com.

asl above see level, *LOI* loss on ignition, *An. met.* analytical methods, *Det. limits* detection limits, *INAA* instrumental neutron activation analysis, *FUS-ICP* fusion-inductively coupled plasma, *TD-ICP* total digestion-inductively coupled plasma

Table 2 Sr-Nd-Pb isotope ratios of representative El Metate samples

Sample no.	Flow unit	$^{87}Sr/^{86}Sr$	1 sd*	1 SE(M)	Number of runs per sample	$^{143}Nd/^{144}Nd$	1 sd*	1 SE(M)	Number of runs per sample	εNδ	1 s	$^{206}Pb/^{204}Pb$	1 sd %	$^{207}Pb/^{204}Pb$	1 sd %	$^{208}Pb/^{204}Pb$	1 sd%	Number of runs per sample
14285	F1	0.704007	33	4	56	0.512791	15	2	66	2.98	0.29	18.6890949064	0.022	15.5912415626	0.022	38.4667089148	0.022	95
14282	F4	0.703831	35	4	59	0.512789	17	2	67	2.95	0.33	18.6542073662	0.023	15.5831109296	0.022	38.4131303312	0.024	99
1205	F4b	0.703767	32	4	58	0.512819	15	2	67	3.53	0.29	18.6383676209	0.025	15.5832113078	0.024	38.393025797	0.025	99
14268	F5	0.703127	34	4	57	0.512942	16	2	67	5.93	0.31	18.5435296523	0.025	15.5547039033	0.024	38.2099740133	0.025	98
1210	F11	0.703303	34	4	58	0.512870	13	1	67	4.53	0.25	18.5957607111	0.022	15.5662473946	0.023	38.3024548705	0.023	95
14308	F12	0.703727	38	5	57	0.512797	16	2	68	3.10	0.31	18.6287434718	0.023	15.5766867258	0.023	38.3681966973	0.023	98

Between 60 and 70 isotopic ratios were determined for Sr and Nd on each sample. Sr and Nd isotopic ratios were corrected for mass fractionation by normalizing to $^{87}Sr/^{86}Sr = 0.1194$ and to $^{143}Nd/^{144}Nd = 0.7219$. Isotopic values were adjusted with the Sr standard NBS 987: $^{87}Sr/^{86}Sr = 0.710242 \pm 12$ ($\pm 1\sigma_{abs}$, $n = 31$) and with the Nd standard La Jolla: $^{143}Nd/^{144}Nd = 0.511846 \pm 7$ ($\pm 1\sigma_{abs}$, $n = 24$). Ninety isotopic ratios were determined for Pb on each sample. Pb isotopic ratios were corrected by comparison of the mean values from the laboratory with the standard NBS 981: $^{206}Pb/^{204}Pb = 16.89 \pm 0.07$ %, $^{207}Pb/^{204}Pb = 15.43 \pm 0.11$ %, and $^{208}Pb/^{204}Pb = 36.53 \pm 0.15$ % ($\pm 1\sigma_{rel}$, $n = 26$). Total blanks during analyses of these samples were 0.23 ng for Sr and Nd and 850 pg for Pb. Further details of the analytical procedures are described in the LUGIS website at http://www.geofisica.unam.mx/laboratorios/universitarios/lugis/index.html

*1 sd** standard deviation on the last two digits, 1 SE(M) = 1sd/$n - 2$

Table 3 Modal mineralogical analyses (vol%) of El Metate rock samples

Sample no.		14285	14286-C	14266	14281	14282	1205	14268	14300	14298	14305	14288	14287	1203	15333	15334	14309	1209	14302	14270	1210	14308	14328	14299	15331
Flow unit		F1	F1	F2	F3	F4	F4b	F5	F5 ?	F6	F6	F6	F6	F6	F6	F6	F7	F8	F9	F10	F11	F12	F13	Dome	Dome
Phenocryst	Ol	5.9	6.6	–	–	–	2.4	–	–	–	–	–	–	–	–	–	–	–	–	–	–	–	–	–	–
	Plag	13.0	12.7	11.03	12.1	5.6	11.1	14.6	6.6	12.3	2.4	3.7	2.6	16.9	4.1	2.6	4.4	3.7	8.0	8.0	5.0	4.9	2.5	10.7	0.7
	Cpx	–	–	2.64	1.7	2.9	1.6	2.7	0.6	0.7	0.6	–	0.2	2.0	0.2	0.2	0.2	1.2	–	0.3	1.0	–	–	0.1	0.6
	Opx	–	–	0.34	1.7	–	2.1	–	–	0.2	–	0.1	–	0.1	–	–	0.2	0.1	0.2	–	–	–	0.2	–	–
	Hbl	–	–	—	–	–	–	1.3	1.2	1.5	2.6	1.8	2.1	2.0	1.2	2.1	1.6	1.9	6.3	4.5	1.8	1.7	1.8	5.5	1.9
Microphenocryst	Plag	27.1	27.4	12.5	18.2	19.5	14.0	13.4	28.8	20.5	34.4	30.8	34.9	21.0	26.7	34.9	30.6	26.3	15.2	18.5	16.7	30.8	28.4	13.3	26.4
	Px	3.9	11.5	11.8	6.8	6.8	8.7	5.9	13.5	12.4	6.7	6.1	6.1	12.2	8	9.1	7.3	13.3	3.0	0.2	6.0	8.3	8.3	3.0	4.0
	Ox	0.5	–	–	–	–	–	2.0	4.5	0.7	1.4	1.4	0.3	1.1	1.2	0.5	0	1.0	0.3	0	0.7	0	0.7	0.3	1.6
Groundmass		50.5	41.9	61.6	59.5	65.1	59.9	62.0	49.5	51.5	51.9	56.1	53.8	44.4	52.4	58.2	55.6	53.0	67.3	68.4	69.4	54.3	58.7	67.4	66.4
% Vesicles		0.1	0.6	8.7	0.0	0.6	8.0	4.2	17.8	5.9	2.2	0.4	0.1	2.4	9.4	6.5	8.7	2.0	5.5	6.5	11.3	28.9	13.1	20.4	12.4

Geographic coordinates are listed in Table 1, and sampling locations are indicated in Fig. 2. 1000 points per thin section (4.2 cm^2) were counted and recalculated to dense rock equivalent (DRE). The volume (%) of vesicles is also given. Phenocrysts are crystals >0.2 mm, microphenocrysts are crystals between 0.02 and 0.2 mm, and groundmass includes glass and microlites that could not be optically identified

Ol olivine, *Plag* plagioclase, *Cpx* clinopyroxene, *Opx* orthopyroxene, *Hbl* hornblende, *Px* pyroxene (includes both Cpx and Opx), *Ox* oxides

Table 4 Average mineral and glass compositions of El Metate lavas

Mineral	Olivine								Plagioclase															
Sample #	14285		14285		1205		1205		14285		14285		14282		1205		1205		14268		14268		14298		14298	
Flow unit	F1		F1		F4b		F4b		F1		F1		F4		F4b		F4b		F5		F5		F6		F6	
Crystal type	ph core		ph rim		ph core		ph rim		ph		micro		mph		ph		micro		mph		micro		ph/mph		micro	
n	*10*	*stdev*	*10*	*stdev*	*11*	*stdev*	*11*	*stdev*	*11*	*stdev*	*8*	*stdev*	*7*	*stdev*	*10*	*stdev*	*8*	*stdev*	*15*	*stdev*	*9*	*stdev*	*16*	*stdev*	*6*	*stdev*
wt. %																										
SiO_2	40.10	0.18	39.25	0.67	39.88	0.26	39.42	0.29	52.92	1.94	53.30	2.55	54.52	0.89	51.86	1.03	53.70	1.99	53.87	1.55	55.15	1.49	52.92	2.43	53.36	1.01
TiO_2	0.01	0.00	0.01	0.01	0.01	0.01	0.00	0.01	0.03	0.02	0.04	0.03	0.03	0.01	0.02	0.01	0.03	0.02	0.03	0.01	0.06	0.03	0.03	0.02	0.03	0.02
Al_2O_3									28.64	1.37	28.40	1.61	27.01	0.57	28.79	0.34	27.96	1.40	27.39	0.86	26.91	0.85	28.41	1.49	28.24	0.71
FeO	15.75	0.69	20.65	2.23	17.23	1.27	20.14	1.54	0.63	0.11	0.69	0.12	0.80	0.06	0.70	0.03	0.83	0.12	0.75	0.05	0.86	0.11	0.80	0.09	0.83	0.09
MnO	0.33	0.03	0.47	0.06	0.35	0.05	0.47	0.08	0.01	0.01	0.01	0.01	0.01	0.01	0.01	0.01	0.01	0.01	0.00	0.01	0.01	0.01	0.01	0.01	0.00	0.00
MgO	43.60	0.67	40.04	1.76	42.57	0.97	40.47	1.26	0.13	0.02	0.11	0.02	0.08	0.02	0.10	0.01	0.09	0.01	0.09	0.01	0.11	0.04	0.08	0.02	0.08	0.01
CaO									13.60	1.45	12.96	1.83	11.84	0.58	13.63	0.27	12.69	1.49	12.19	0.49	11.58	1.01	12.65	1.75	12.39	0.89
Na_2O									3.15	0.77	3.36	0.95	3.90	0.35	2.94	0.19	3.42	0.69	3.70	0.29	4.02	0.57	3.91	0.90	4.05	0.47
K_2O									0.13	0.07	0.16	0.11	0.22	0.02	0.13	0.02	0.19	0.09	0.17	0.04	0.21	0.08	0.15	0.05	0.16	0.03
P2O5																										
SrO									<0.1	0.03	<0.1	0.05	<0.1	0.12	<0.1	0.00	<0.1	0.11	0.68	0.30	0.84	0.44	0.39	0.29	0.53	0.31
NiO	0.31	0.05	0.22	0.07	0.19	0.03		0.19																		
Total	100.1		100.6		100.2		100.5		99.3		99.0		98.4		98.2		98.9		98.9		99.7		99.4		99.7	

Mineral	Plagioclase				Plagioclase continuation								Clinopyroxene													
Sample #	14309		14309		1210		1210		14308		14308		14285		14282		1205		14268		14298		14308		1210		14309	
Flow unit	F7		F7		F11		F11		F12		F12		F1		F4		F4b		F5		F5		F7		F11		F12	
Crystal type	ph		micro		ph		micro		ph		mph		micro		ph		ph/mph		mph		mph		ph/mph		ph/mph		mph	
n	*19*	*stdev*	*5*	*stdev*	*14*	*stdev*	*13*	*stdev*	*21*	*stdev*	*9*	*stdev*	*6*	*stdev*	*17*	*stdev*	*23*	*stdev*	*10*	*stdev*	*13*	*stdev*	*3*	*stdev*	*25*	*stdev*	*5*	*stdev*
wt. %																												
SiO_2	51.69	2.03	55.46	1.30	53.21	1.51	54.44	1.04	53.55	0.97	54.16	1.25	51.60	0.83	51.48	0.98	52.25	0.69	51.37	0.63	51.52	1.22	51.72	0.58	51.74	1.29	51.61	0.97
TiO_2	0.02	0.02	0.05	0.01	0.02	0.01	0.04	0.01	0.02	0.01	0.02	0.01	1.11	0.30	0.53	0.20	0.46	0.13	0.72	0.30	0.60	0.20	0.60	0.06	0.62	0.47	0.64	0.17
Al_2O_3	29.66	1.35	27.30	0.74	28.60	1.16	27.61	0.70	28.38	0.75	27.66	0.94	2.24	0.24	3.50	0.93	2.96	0.73	4.29	0.47	3.68	1.19	3.70	0.62	3.20	1.67	4.79	1.02
FeO	0.75	0.05	0.89	0.03	0.68	0.12	0.77	0.10	0.63	0.08	0.77	0.05	13.05	2.10	7.81	1.89	6.54	1.09	7.56	1.79	7.20	1.82	8.29	0.69	7.45	0.94	6.01	1.10
MnO	0.01	0.01	0.01	0.01	0.01	0.01	0.01	0.01	0.01	0.01	0.01	0.01	0.32	0.06	0.17	0.05	0.15	0.04	0.16	0.05	0.14	0.05	0.17	0.03	0.17	0.04	0.13	0.05
MgO	0.08	0.01	0.10	0.01	0.09	0.03	0.10	0.02	0.07	0.01	0.08	0.01	15.59	1.74	15.25	1.16	16.28	0.54	14.58	1.19	14.94	1.41	14.61	0.52	15.40	0.56	14.30	0.78
CaO	13.97	1.49	11.25	1.03	13.23	1.15	12.18	0.71	12.62	0.88	11.93	1.00	15.83	1.03	20.27	0.54	20.62	0.77	21.17	0.55	21.41	1.29	21.07	0.69	21.11	0.65	22.12	0.44
Na_2O	3.10	0.84	4.52	0.47	3.33	0.57	3.78	0.35	3.84	0.46	4.21	0.54	0.36	0.18	0.33	0.11	0.25	0.05	0.39	0.07	0.06	0.02	0.04	0.04	0.34	0.08	0.07	0.03
K_2O	0.13	0.06	0.25	0.06	0.10	0.03	0.14	0.03	0.12	0.03	0.15	0.04																
P2O5																												
SrO	0.39	0.35	0.24	0.19	0.32	0.28	0.31	0.26	<0.1	0.18	<0.1	0.05																
NiO																												
Total	99.4		99.9		99.6		99.4		99.2		99.0		100.1		99.4		99.5		100.2		99.6		100.2		100.0		99.7	

Table 4 (continued)

Mineral	Orthopyroxene				Orthopyroxene continuation										Hornblende												Oxide			
Sample #	14285		14282		1205		14268		14298		14308		1210		14309	14268		14298		14308		1210		14309			14298		14309	
Flow unit	F1		F4		F4b		F5		F6		F7		F11		F12	F5		F6		F7		F11		F12			F6		F7	
Crystal type	micro		ph/mph		ph		mph		mph		mph		mph		mph	ph		ph		ph		ph		ph						
wt. %																														
SiO_2	54.09	0.46	54.55	0.77	54.81	1.50	54.51	0.67	54.61	0.24	55.35	0.68	53.66	0.18	54.58	43.48	0.78	42.94	0.61	43.01	1.02	44.36	0.63	42.89	0.49	0.11	0.03	0.35	0.48
TiO_2	0.46	0.06	0.21	0.10	0.21	0.18	0.38	0.07	0.32	0.04	0.17	0.06	0.51	0.05	0.44	2.08	0.40	1.89	0.16	1.74	0.05	1.68	0.13	2.09	0.11	11.88	0.60	14.52	2.08
Al_2O_3	1.49	1.01	1.97	0.55	2.27	1.10	2.55	0.83	2.54	0.17	1.43	0.76	2.65	0.03	2.82	11.47	0.75	11.34	0.46	11.24	0.39	10.89	0.56	11.37	0.36	2.68	1.50	2.147	0.21
FeO	15.76	0.64	13.58	2.18	12.81	4.06	12.86	0.20	12.37	0.27	14.26	0.74	14.50	0.20	10.85	10.23	1.02	10.25	0.62	11.48	1.35	10.05	0.95	11.09	0.86	81.33	4.00	80.02	1.90
MnO	0.36	0.02	0.28	0.06	0.25	0.08	0.35	0.01	0.25	0.02	0.28	0.06	0.32	0.01	0.27	0.09	0.02	0.07	0.02	0.09	0.02	0.09	0.02	0.08	0.02	0.58	0.04	0.65	0.07
MgO	24.92	1.91	28.19	1.49	28.59	6.13	27.85	0.57	27.27	0.08	26.56	0.49	27.48	0.17	24.97	15.54	0.62	15.28	0.50	14.56	1.02	15.93	0.61	14.68	0.57	3.20	1.69	2.71	0.37
CaO	2.93	0.98	1.26	0.19	1.31	9.99	1.74	0.13	1.98	0.30	1.50	0.20	1.72	0.37	6.01	11.49	0.29	12.77	0.27	12.37	0.15	11.22	0.16	12.65	0.15				
Na_2O	0.12	0.20	0.04	0.04	0.05	0.10	0.03	0.01	0.00	0.00	0.02	0.02	0.02	0.00	0.02	2.16	0.15	2.43	0.17	2.23	0.13	2.01	0.08	2.33	0.07				
K_2O																0.59	0.09	0.48	0.08	0.38	0.02	0.45	0.05	0.55	0.04				
P2O5																													
SrO																													
NiO																													
Total	100.1		100.1		100.3		100.3		99.3		99.6		100.9		100.0	97.1		97.4		97.1		96.7		97.7		99.8		100.4	

ph phenocryst, *mph* microphenocryst, *micro* microlite, *n* number of analyzed points, *stdev* standard deviation

microgranular assemblage of pyroxene + plagioclase + oxide + glass and/or opacite (Fig. 5c, d), whereas others are fully replaced by these materials, forming mineral ghosts (Fig. 5d). Enclaves consisting of coarser tabular plagioclase + destabilized pyroxene + melt are rarely found.

Major and trace element contents

Based on the classification of LeBas et al. (1986), El Metate's lavas are calc-alkaline basaltic andesites to andesites (57 to 62 wt% SiO_2, Table 1). Our results are in general agreement with previously published data (Fig. 6, Hasenaka et al. 1994; Losantos et al. 2014).

In spite of their similar SiO_2 and $Na_2O + K_2O$ contents (Fig. 6), early and late lavas display distinct trends in major element plots (Fig. 7). Late lavas have distinctly higher Al_2O_3, CaO, Na_2O, and Sr and lower Fe_2O_{3T}, MgO, TiO_2, and Ni at a given SiO_2 weight percent content than early lavas, although the most evolved units of both groups have similar compositions. In early lavas (F1 to F4), Fe_2O_{3T}, MgO, TiO_2, and Ni sharply decrease while CaO slightly decreases, Al_2O_3 displays a scattered pattern, and K_2O increases constantly with increasing SiO_2. In contrast, late lavas (F5 to F13) show a tendency to decrease in Al_2O_3, a sharp decrease in CaO, weak decreases in Fe_2O_{3T} and MgO, constant Ni, and variable K_2O with increasing SiO_2.

The trends observed in late lavas indicate a general progressive increase in the degree of differentiation of the flows with the emplacement sequence from F5 to the formation of the final summit dome. Also, sampling along the longest lava units (F5, F6) reveals some systematic variations in major elements with distance from the vent (<2 wt% SiO_2). As noted above, the emplacement sequence could not be constrained for early lavas, except that unit F4b was emplaced by a late breakout from unit F4. Unit F4b is less evolved than F4, the opposite of what would be expected if differentiation increased over time.

Interestingly, Sr contents in the most mafic (<59 wt% SiO_2) late lavas (F5, F6, F7, F8) are abnormally high (>1300 ppm), decrease in more evolved subsequently erupted units (F9, F10, F11), and are lowest in the most silicic and last erupted lavas (F12 and F13 with ~800 ppm) which are similar in this respect to early lavas (F2–F4; Fig. 7).

Early and late lavas have also distinct trace and rare earth element (REE) patterns (Fig. 8). Although both groups span similar ranges in light REE and are depleted in heavy REE, the late lavas show a stronger depletion (Fig. 8a). Also, late lavas show a marked decrease in REE with increasing SiO_2, whereas early lavas show constant to slightly increasing REE with SiO_2 (La shown as an example in Fig. 7). The elevated Sr and lower Y contents of late lavas yield higher Sr/Y ratios (60–140) than early lavas (<50). Both lava groups show trace element patterns typical for arc lavas but early lavas are less depleted in Ta and Nb and slightly more enriched in large ion lithophile elements (LIL) than late lavas (Fig. 8b). None of the samples shows a Eu anomaly.

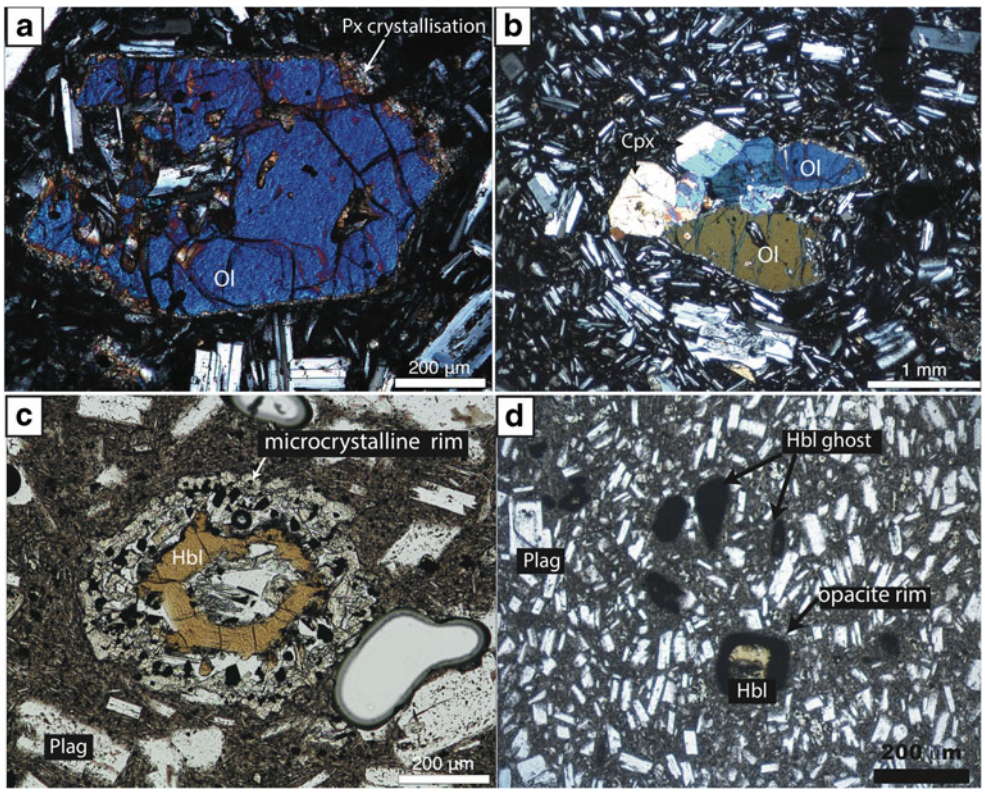

Fig. 5 Photomicrographs under crossed polars of El Metate lavas: **a** olivine (*Ol*) phenocryst with reaction rim of microcrystalline pyroxene (sample no. 14286, F1). **b** Cluster of olivine and augite (*Cpx*) phenocrysts (sample no. 1205, F4b). **c** Brown hornblende with thick microcrystalline reaction rim (gabbroic-type; sample no. 14268, F5). **d** Hornblende (*Hbl*) with opacite-rim (black-type) and hornblende ghost embedded in a seriate groundmass consisting mostly of plagioclase (*Plag*) and some orthopyroxene microlites and glass (sample no. 14287, F6)

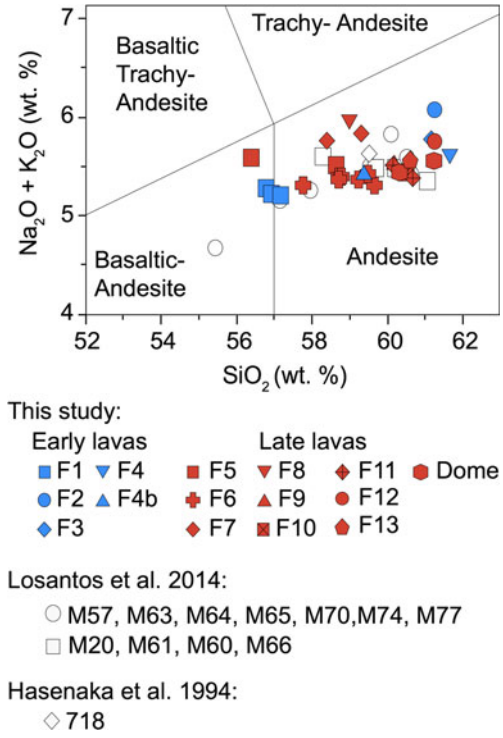

Fig. 6 Total alkalies ($Na_2O + K_2O$) vs. SiO_2 diagram after LeBas et al. (1986) for all analyzed volcanic rocks. Data from Losantos et al. (2014; the two different symbols represent two distinct groups representing different crystallization trends) and Hasenaka et al. (1994) for El Metate lavas are also plotted

Isotopic composition

The first Sr-Nd-Pb isotope dataset of six samples representative of the chemical diversity of El Metate lavas (three samples from each lava group) is reported in Table 2. The variations measured are significant and nearly cover the entire range of MGVF products (Fig. 9). Early lavas are isotopically quite homogeneous ($^{87}Sr/^{86}Sr$ 0.704007–0.703767, $^{143}Nd/^{144}Nd$ 0.512789–0.512819, $^{206}Pb/^{204}Pb$ 18.63836–18.68909, $^{207}Pb/^{206}Pb$ 15.5831–15.5912), while the late lavas cover a wider range ($^{87}Sr/^{86}Sr$ 0.703127–0.703727, $^{143}Nd/^{144}Nd$ 0.512797–0.512942, $^{206}Pb/^{204}Pb$ 18.54352–18.62874, $^{207}Pb/^{206}Pb$ 15.5547–15.5766). The small isotopic variations of the early lavas do not correlate with SiO_2. In contrast, variations in late lavas correlate with the inferred eruption sequence and SiO_2 contents. Late lavas become more radiogenic and more SiO_2 rich over time, and the last, most silicic eruptive unit (F12) is isotopically similar to the early lavas (Fig. 9a). All the data follow a linear trend in plots of $^{87}Sr/^{86}Sr$ ratios vs. εNd (Fig. 9c) and $^{206}Pb/^{204}Pb$ vs. $^{207}Pb/^{204}Pb$ (Fig. 9d). The earliest unit of the late lavas (F5) is only slightly less radiogenic than the subducting oceanic crust (MORB-COCOS), whereas the last erupted lava (F12) and the early lavas (F1, F4, F4b) both plot toward values reported for the granodioritic upper crustal basement.

Thermobarometry and hygrometry

Crystallization pressure (*P*), temperature (*T*), and water content (H_2O) were estimated for the different lava units. We applied the olivine-liquid thermometer (based on Beattie 1993) and the two-pyroxene thermobarometer (based on Brey and Köhler 1990) using the equations of Putirka (2008), the hornblende thermobarometer and hygrometer from Ridolfi et al. (2010), and the plagioclase-liquid hygrometer from Waters and Lange (2015). Details of the methods and tests for equilibrium are given in Online resource 1, and the results are presented in Table 5 and Fig. 10. Assuming a maximum pressure of crystallization of 8 kbar (~24 km; Hasenaka and Carmichael 1987), dry conditions (olivine composition is weakly affected by H_2O), and equilibrium between mineral core and bulk rock, olivine phenocrysts in the most mafic early lava (F1) are constrained to have formed at 1176 ± 35 °C, whereas olivines in more evolved early lava (F4b) crystallized at 1135 ± 35 °C. The lowest temperature of olivine growth was estimated at 1065 °C for the most mafic early lava (F1) and 1081 °C for the more evolved early lava (F4b), assuming dry conditions, a pressure of 5 kbar (corresponding to the highest pressure estimated for pyroxene crystallization, Fig. 10), and using the compositions of olivine rims and a residual melt calculated by subtracting the mineral core composition from the bulk rock. Two-pyroxene microphenocrysts in the most mafic early lava (F1) formed at 1076 ± 35 °C and between 2.5 and 4.4 ± 2.8 kbar, whereas pyroxenes forming rims around olivine yield slightly higher T (~1100 °C) and low P (1 atm). Pyroxenes in more evolved early lavas (F4 and F4b) formed at lower *T* (in average 988 ± 35 °C) and over a larger *P* range (2.3–5.5 ± 2.8 kbar). In comparison, two-pyroxene phenocrysts and microphenocrysts in the late lavas formed over an even wider *P-T* range that extends to lower *P* and *T* (0–4 ± 2.8 kbar; 938–987 ± 35 °C). [Note that the Putirka (2008) model is also valid for hydrous melts (K. Putirka, personal communication)]. The crystallization conditions of hornblende in late lavas are constrained at 2.7–3.1 ± 0.4 kbar and 922–972 ± 22 °C. Results from the hornblende hygrometer yield a water content of 5.5–6.1 ± 1 wt% H_2O. Two-pyroxene microlites at hornblende rims formed at a *P-T* range of 0–3 ± 2.8 kbar and 910–1040 ± 38 °C. Water contents were also estimated with the plagioclase-liquid hygrometer using the plagioclase phenocryst compositions. For early lavas, we used on the one hand the previously calculated crystallization *T* of olivine cores at 8 kbar and bulk rock composition and, on the other hand, the previously calculated crystallization *T* of olivine rims at 5 kbars and a recalculated residual melt composition (see above and Table 5). Both condition sets yield 1.9 to 3.5 ± 0.35 wt% H_2O. In the case of the late lavas, this method yields 4.5 to 5.5 ± 0.35 wt% H_2O at the *P* and *T* conditions obtained from the hornblende thermobarometer and considering equilibrium of the minerals with the bulk rock.

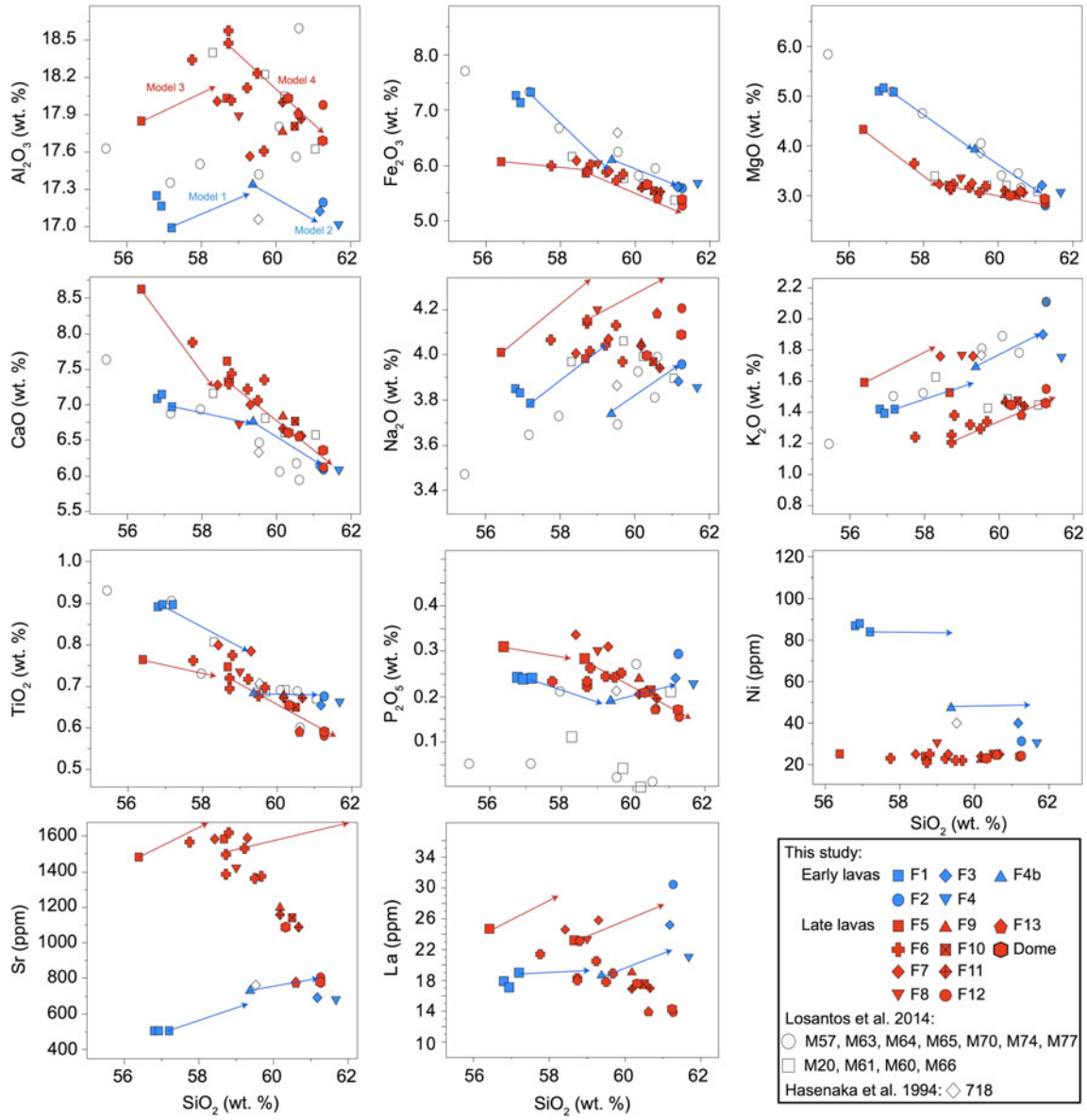

Fig. 7 Harker diagrams showing selected major (in wt%) and trace (in ppm) elements plotted against silica. Data from Losantos et al. (2014; the two different symbols represent their two crystallization trends) and Hasenaka et al. (1994) for El Metate lavas are also plotted. *Arrows* represent modeling of fractional crystallization for both lava groups (proportions in wt%): model 1: 3.3 olivine, 5.5 plagioclase, 0.3 clinopyroxene, 1.6 Ti-Fe oxide, 0.18 apatite; model 2: 2.7 olivine, 8.8 plagioclase, 0.9 clinopyroxene, 0.7 Ti-Fe oxide; model 3: 8 hornblende, 8 plagioclase, 4 cpx, 0.2 apatite; model 4: 6 hornblende, 10 plagioclase, 1.1 Ti-Fe oxide, 0.35 apatite

In summary, mineral-melt equilibria indicate that the magmas feeding the two lava groups followed a distinct crystallization history during ascent. The magma feeding the early lavas crystallized olivine at high *T* and plagioclase at moderate water contents (<3.5 wt% H_2O), followed by minor pyroxene crystallization. In contrast, the late lavas were fed by a magma that crystallized hornblende, pyroxene, and plagioclase at lower *T* (900–1000 °C) and higher H_2O (<6 wt%). In both cases (early and late lavas), mineral crystallization depths are poorly constrained (0–15 km) except for hornblendes in the late lavas, which formed at depths of ~7–10 km.

Magma and lava rheology

The viscosity of the magma and lava can be estimated on the basis of petrological and geochemical parameters (petrological approach, see details in Online resource 2). This approach considers that the interstitial melt has a Newtonian rheology that depends on *T*, melt composition, and H_2O content, while the content and shape of crystals and bubbles account for the deviation of the mixture from this behavior. Here, the melt viscosity is calculated using the model of Giordano et al. (2008). The effect of crystals is taken into

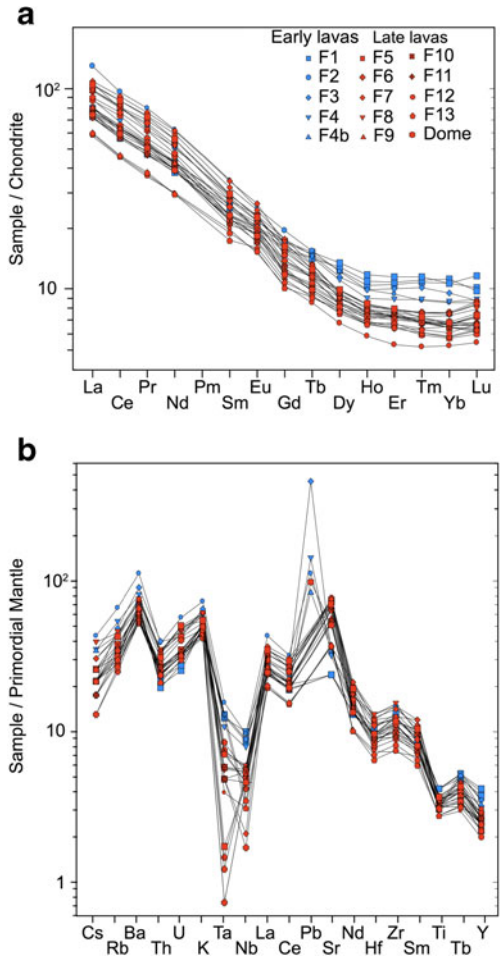

Fig. 8 **a** Chondrite-normalized (Sun and McDonough 1989) REE compositions of analyzed rocks from El Metate shield. **b** Trace element abundances of analyzed rocks from El Metate shield normalized to primordial mantle (McDonough et al. 1992)

account considering two populations of crystals and applying the equation of Krieger and Dougherty (1959); Eq. 2, Online resource 2) with the fitting parameters of Mueller et al. (2010). The effect of vesicles is complex (Manga et al. 1998) and briefly discussed below.

Using this approach, the pre-eruptive viscosity of the magma that fed the lava flows was estimated from a recalculated melt composition (calculated by subtracting the composition of the phenocrysts from the whole rock, Online resource 3), the H_2O content obtained from hygrometry, the crystallization T of phenocrysts obtained from geothermometry, and the amount of phenocrysts in the lavas. The calculated viscosities (Table 6; Online resource 4) vary from 3×10^2 Pa s for the most mafic early lavas (F1, 1176 °C, 1.9 wt% H_2O, 19 vol% crystals) to 7×10^3 Pa s for the most evolved early lavas (F4, 989 °C, 1.9 wt% H_2O, 9 vol% crystals) and from 7×10^2 to 10^3 Pa s for the late lavas (922–972 °C, 4.5–5.5 wt% H_2O, 6–19 vol% crystals).

The viscosity of the lavas upon eruption was calculated using the same approach, assuming a low dissolved water content (0.1 wt% H_2O), the crystallization T of microphenocrysts, and the amount of microphenocrysts + phenocrysts in the lava. The results vary between 3×10^6 and 2×10^7 Pa s for the early lavas (987–1076 °C, 40–50 vol% crystals) and between 4×10^7 and 10^8 Pa s for the late lavas (922–972 °C, 31–48 vol% crystals; Table 6, Online resource 4). These are minimum values since the amount of microlites has not been taken into account. The lower viscosity value of the early lavas compared to the late lavas is in agreement with the observed thinner flow front of the early lavas in contrast to the thicker blocky front of the late lavas. Assuming dry interstitial melt increases the values by 0.2 to 0.4 log units depending on the SiO_2 content. Proximal lavas contain up to 30 vol% bubbles, which can increase or decrease the viscosity by 0.6 to 0.7 log units depending on the capillary number of the bubbles (Fig. 5 in Rust and Manga 2002).

The bulk apparent viscosity of the flows is however likely to be several orders of magnitude larger than the viscosity of the molten lava given by petrological estimates in particular because of the formation of a resistant crust (e.g., Griffiths and Fink 1993; Kerr et al. 2006; Castruccio et al. 2013). Several rheological models have been developed to extract the apparent viscosity of the flows from their dimensions (e.g., Nichols 1939; Hulme 1974; Griffiths and Fink 1993; Pinkerton and Wilson 1994). We have applied some of these models (see Online resource 2) to the latest flows (F6, F7, F8, and F11) because these are fully exposed, which allows measuring their dimensions entirely. The average flow width and thickness required in the equations were derived from 7 to 9 profiles drawn across each of these flow units (Fig. 11) and the total flow length represents an average of 10 vent-front measurements. The underlying slope was approximated from the slope of the flow surface over the entire length of the flow because the pre-eruption topography is buried under adjacent flows. This represents a minimum value, as lavas tend to fill depressions and lower slope gradients. The thermal diffusivity used for the calculations is 4.21×10^{-7} m^2 s^{-1}, as in Kilburn and Lopes (1991). Note that error propagation for these models (calculated following Chevrel et al. 2013, Appendix A.2, and Lefler 2011) yields up to 40 % error due to the large standard deviation obtained from flow heights (up to 10 %). Physical constants, dimensions, and rheological parameters calculated by this approach are given in Table 7 and presented below.

The simplest rheological model used is the one originally defined by Nichols (1939) who adapted the equation of Jeffreys (1925) to describe channelized lava flowing down an inclined slope. The derived equation assumes Newtonian rheology and requires knowledge of the flow mean velocity (Eq. 6 in Online resource 2). This was derived from the flow dimensions, following the G_z approach developed by Pinkerton and Sparks (1976), Hulme and Fielder (1977), and

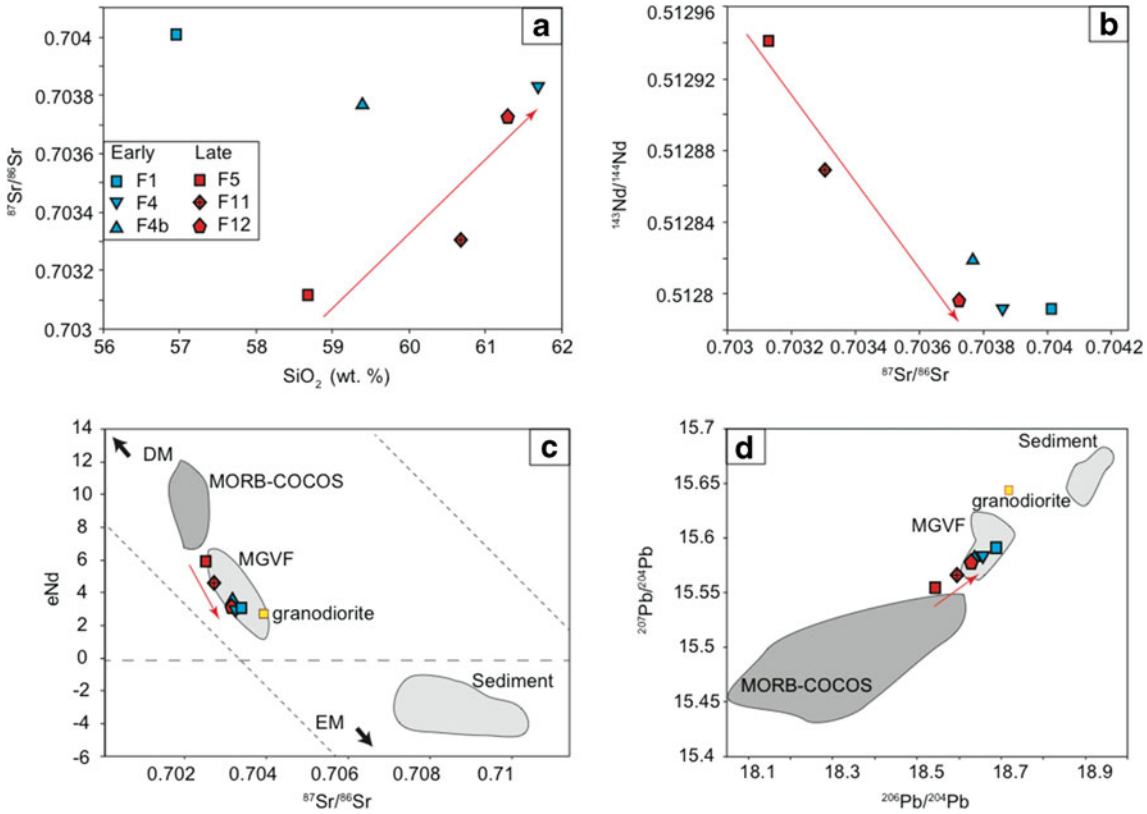

Fig. 9 Isotopic ratios (Sr-Nd-Pb) for six selected samples from El Metate (see also Table 2). **a** $^{87}Sr/^{86}Sr$ ratio vs. SiO_2. **b** $^{87}Sr/^{86}Sr$ ratio vs. $^{143}Nd/^{144}Nd$. **c** εNd vs. $^{87}Sr/^{86}Sr$ ratio. **d** $^{206}Pb/^{204}Pb$ vs. $^{207}Pb/^{204}Pb$. Field for the MORB-COCOS rocks after Class and Lehnert (2012), MGVF field after Blatter and Hammersley (2010), oceanic sediment data from Verma (2000), and granodiorite analysis from sample of the local basement in the Jorullo area. *DM* depleted mantle, *EM* enriched mantle. *Red arrows* indicate the temporal evolution of the late lavas

Pinkerton and Wilson (1994) and assuming cooling-dependent flow advance (results from these calculations are presented below). Applying the Jeffreys' equation yielded apparent viscosities of 6×10^9 Pa s for F7, ~10^{10} Pa s for F6 and F8, and slightly higher for F11 (10^{11} Pa s).

Hulme (1974) developed equations describing the unconfined flow of ideal Bingham liquids on an inclined plane. These predict the formation of lateral levées and a simple relation between yield strength and flow dimensions. Based on this theory, Wilson and Head (1983) derived an equation that relates the apparent viscosity of the flow within the channel to the effusion rate and yield strength (Eq. 9 in Online resource 2). For unit F6, the occurrence of a well-developed channel allowed us to apply this equation, giving an apparent viscosity of 6×10^8 Pa s.

Considering a Bingham model, bulk yield strength of the flows can be estimated from their thickness (Eq. 7 in Online resource 2). This yielded values of ~10^5 Pa for all lava units, except for F8, which had lower yield strength (8.4×10^4 Pa). For unit F6, Hulme's equation gave a similar value (1.9×10^5 Pa).

The effusion rates estimated from the G_z approach mentioned above are 20 and 60 m^3/s for units F7 and F6, respectively, corresponding to a lava front advance of ~30 m/day. For F8 and F11, the effusion rate was estimated at 9–12 m^3/s, equivalent to a lava front advance of a few meters per day. These values were then used to derive emplacement times, considering the individual lava flow volumes that range between 0.5 and 2.2 km^3 (Table 7). This yields emplacement times of between ~500 days for F6 and F8, ~330 days for F7, and ~2300 days for F11 (t_{Gz} on Table 7). Note that this model assumes a constant effusion rate and therefore underestimates the emplacement duration of the lava flow.

Finally, we applied the model of Kilburn and Lopes (1991) who consider the flow as a Newtonian fluid whose expansion is controlled by the resistance of a cooling crust, hence approximating a Bingham rheology. The equation they derive allows calculation of the emplacement duration of a flow-field based only on its final dimensions and the underlying slope (Eq. 11 in Online resource 2). Applying this equation yields slightly higher values for F6 (600 days) and F11 (~2600 days) but a lower value for F7 (265 days) and a much higher value for F8 (~1300 days). An average of the emplacement times gives 1.5, 0.8, 2.5, and 6.7 years for F6, F7, F8, and F11, respectively (Table 7).

Table 5 Results of thermobarometry and hygrometry

Sample no.	Flow unit	Olivine-liquid (Eq. 22 from Putirka 2008)					CPX-OPX pair (Eq. 37 and 39 from Putirka 2008)					Amphibole (Ridolfi et al. 2010)								Plagioclase-liquid (Waters and Lange 2015)							
		n	Liquid composition	*T* (°C)	stdev	*P* (kbar)	*n*	*T* (°C)	stdev	*P* (kbar)	stdev	*n*	*n**	*T* (°C)	sdev	*P* (kbar)	stdev	H_2O wt%	stdev	*n*	*n**	*T** (°C)	*P** (kbar)	Liquid composition	H_2O wt%	stdev
14285	F1	10 (core)	Whole rock	1176	2	8	5 (micro)	1076	5	3.5	0.8									4	6	1176	8	Residual melt	1.9	0.08
14285	F1	5 (rim)	Residual melt	1065	2	5	6 (Ol rim)	1098	11	0.0	0.0									4	6	1065	5	Residual melt	3.5	0.08
1205	F4b	11 (core)	Whole rock	1135	3	8	9 (ph + micro)	987	21	3.6	1.2									5	6	1135	8	Residual melt	1.9	0.02
1205	F4b	6 (rim)	Residual melt	1081	3	5														5	6	1081	5	Residual melt	2.6	0.02
14282	F4						16 (ph + - micro)	989	17	4.1	0.9									6	7	989	4.2	Whole rock	3.6	0.07
14268	F5						16 (mph)	971	26	1.6	1.3	6	23	946	11	3.1	0.4	5.5	0.3	5	10	946	3.1	Whole rock	5.2	0.03
14298	F6						6	946		0.63		5	12	972	11	3.2	0.4	5.5	0.5	4	9	972	3.2	Whole rock	4.7	0.1
14309	F7						1	894		0		5	14	967	9	3.2	0.2919825726	5.6	0.3	3	13	967	3.2	Whole rock	4.5	0.1
1210	F11						7 (hb rim)	979	7	0.9	0.6	6	17	922	9	2.7	0.4	5.7	0.5	6	10	922	2.7	Whole rock	5.5	0.07
14308	F12						1	966		1.16		3	23	953	11	3.1	0.3349560393	6.1	0.5	3	12	953	3.1	Whole rock	4.8	0.04

Details of the models used, test for equilibrium, and residual melt calculations are presented in Online resource 1. Refer to previous tables for abbreviations. *T** and *P** used in plagioclase-liquid hygrometer are taken from olivine-liquid thermometer for F1 and F4b, from two-pyroxene thermobarometer for F4, and from hornblende thermobarometer for F5, F6, F7, F11, and F12

n number of analyzed grains, *n** number of analyzed points

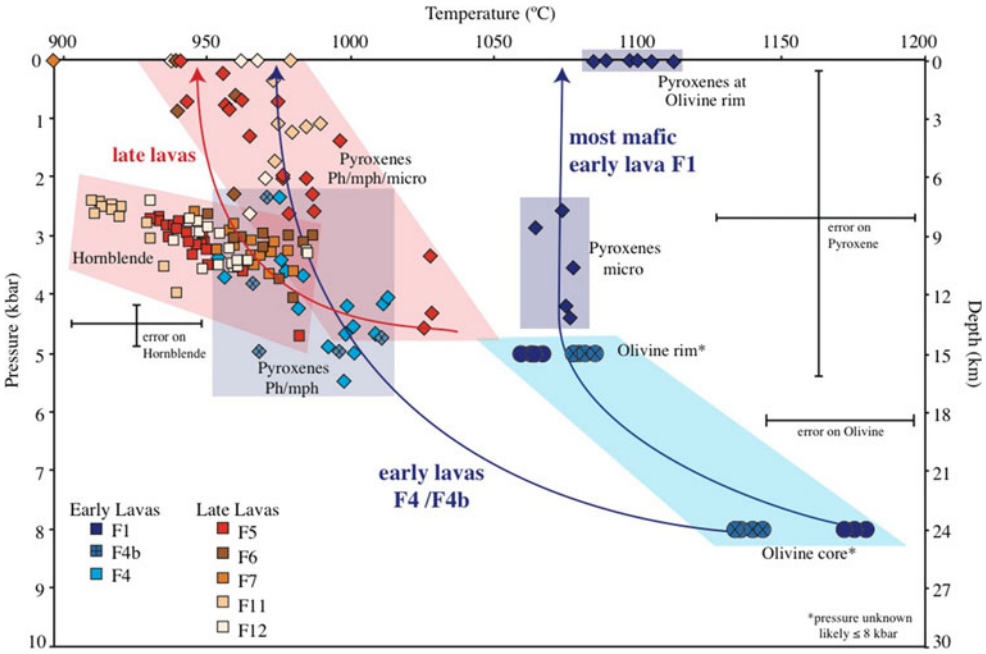

Fig. 10 Pressure-temperature diagram showing results of different mineral-equilibrium thermobarometry methods applied in this study (see also Table 5). Data obtained by the olivine-liquid thermometer (assuming dry condition and pressure at 8 and 5 kbars), the two-pyroxene thermobarometer, and hornblende thermobarometer are plotted as *circles*, *diamonds*, and *squares*, respectively. Representative uncertainties for each model are indicated. The errors given here are inherited from the models applied. *Arrows* indicate *P-T* path of early (*blue*) and late (*red*) lavas

Discussion

Magma source and evolution

Our data allows us to distinguish at least two different magma batches at El Metate that produced the early and late lava groups, respectively. SiO_2 contents in both groups vary over a similarly wide range; nevertheless, they have distinct morphologies, mineralogy, major element trends as a function of SiO_2, trace element concentrations, and isotope compositions. Their mineral assemblages also formed under different conditions, revealing separate evolutionary histories. We consider below some of the processes that may have caused the chemical variations.

Fractional crystallization modeling

Fractional crystallization may have caused the compositional trends observed within each group (Fig. 7). To test this, we first modeled major element trends using a mass balance approach, employing a least-square fit model (Herrmann and Berry 2002) and a specially designed spreadsheet. Parameters used as input were the least evolved whole rock compositions of each trend observed, average compositions for phenocryst phases measured in these same samples, Fe-Ti oxide compositions measured in late lavas, and a representative composition for apatite from the literature (details in Online resource 5). Results are plotted along with the data in Fig. 7. The observed variations in the two groups of lava can

Table 6 Magma and lava viscosities estimated from petrological data and groundmass composition

Sample no.	Flow unit	Pre-eruptive condition					Syn-eruptive condition 0.1 wt% H_2O			
		T (°C)	wt% H_2O	Melt viscosity (Pa s)	Relative viscosity	Bulk viscosity (Pa s)	*T* (°C)	Melt viscosity (Pa s)	Relative viscosity	Bulk viscosity (Pa s)
14285	F1	1176	1.9	1E + 02	2.8	3E + 02	1076	8E + 03	309	3E + 06
14282	F4	989	1.9	5E + 03	1.5	7E + 03	989	9E + 05	22	2E + 07
1205	F4b	1135	3.6	9E + 01	2.5	2E + 02	987	1E + 06	13	2E + 07
14268	F5	946	5.2	5E + 02	3.2	2E + 03	946	6E + 06	19	1E + 08
14298	F6	972	4.7	4E + 02	2.5	1E + 03	972	2E + 06	55	1E + 08
14309	F7	967	4.5	5E + 02	1.4	7E + 02	967	5E + 05	76	4E + 07
1210	F11	922	5.5	7E + 02	1.6	1E + 03	922	6E + 06	8	4E + 07
14308	F12	953	4.8	6E + 02	1.5	9E + 02	953	3E + 06	30	8E + 07

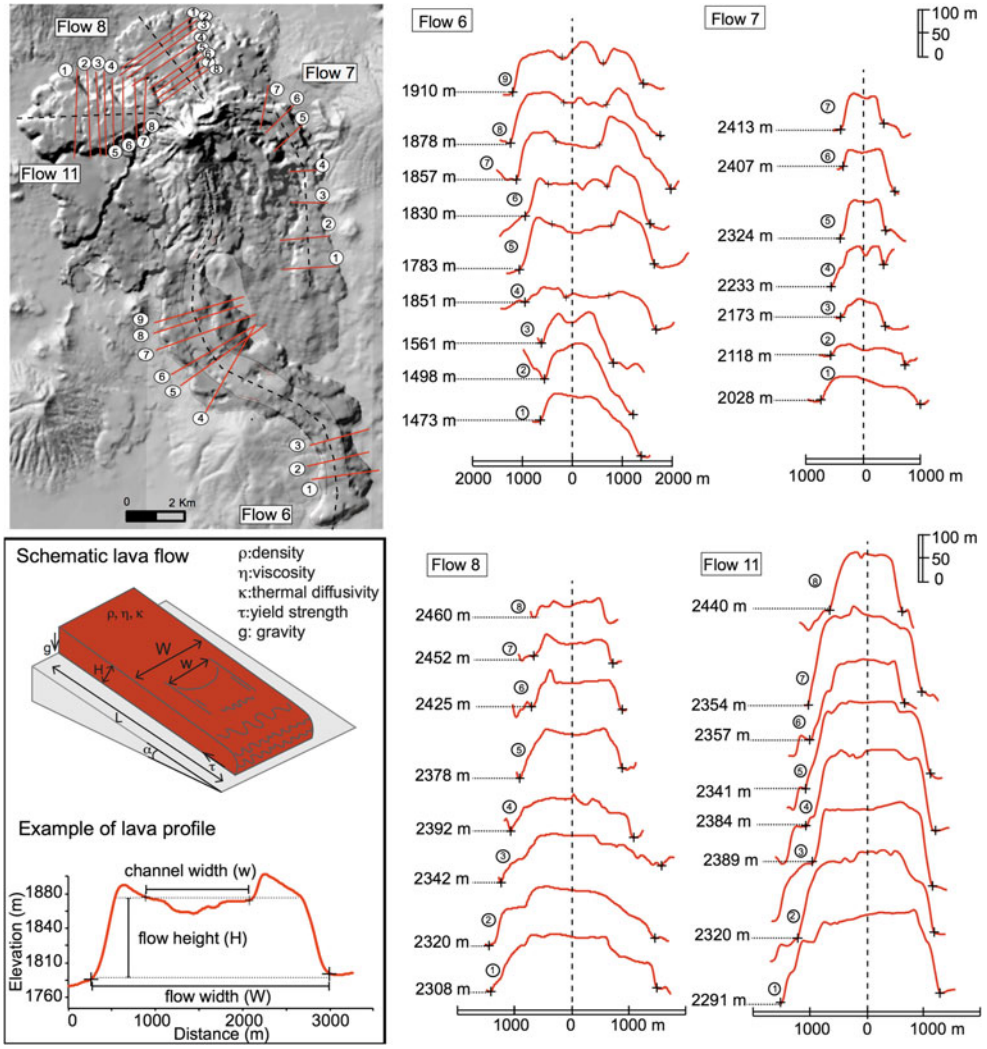

Fig. 11 Topographic profiles (perpendicular to flow direction) across well-exposed El Metate lava flows (F6, F7, F8, and F11) from which width, thickness, and channel width in the case of F6 were estimated

be modeled for most of the elements by fractionation of a combination of the mineral phases present in the samples, namely olivine, plagioclase, clinopyroxene, apatite, and Fe-Ti oxides for early lavas and plagioclase, hornblende, clinopyroxene, apatite, and Fe-Ti for late lavas (Fig. 7). The models however fail to reproduce the variations of Na_2O (Fig. 7). Some discrepancies in TiO_2 for early lavas may be due to higher Ti/Fe ratios in these lavas compared to late lavas.

To further test these results, modeling of selected trace element abundances was undertaken using the mineral assemblages determined by major element modeling, the Rayleigh fractionation equation, and a range of partition coefficients taken from recent literature (Tiepolo et al. 2007; Sisson 1994; Laubier et al. 2014; Prowatke and Klemme 2006; Tepley et al. 2010). For early lavas, the calculations reproduce fairly well the slight increase of REE elements with increasing SiO_2 that is observed. However, the sharp decrease in Ni with increasing SiO_2 could not be reproduced because of the low fractionating amounts of olivine (~3 wt%). This trend would require 15 wt% olivine fractionation, which is inconsistent with major element trends, and may suggest mixing with a source having lower Ni contents. For late lavas, the calculations fail to reproduce the sharp decrease of most REE (e.g., La, Gd) with respect to SiO_2 because these elements are incompatible in all the mineral phases fractionating, except for apatite, which fractionates in too small proportions (<0.4 wt%) to cause a significant effect. Furthermore, the sharp decrease in Sr with increasing SiO_2 would require fractionation of 70 wt% of plagioclase instead of the 6 wt% modeled using major element trends. In conclusion, although fractional crystallization can explain most of the observed variations in the compositions of early lavas, it fails to reproduce trace element variations in late lavas.

The evolution of late lavas with time may instead reflect progressive mixing with the most evolved member of the early lavas (F4). This could explain the convergence of both groups in isotopic, most major element, and some trace element (Sr, Ni) graphs (Figs. 7 and 9), but cannot account for the progressive depletion of late lavas in REE with increasing SiO_2 given that the early lavas have high REE contents.

Table 7 Geometric flow parameters, viscosities, yield strengths, and emplacement durations of El Metate lava flows calculated from the morphological approach

Physical constant				
Denstity ρ [kg/m^3]	2600 ± 100			
Gravitational acceleration g [m/s^2]	9.81			
Grätz number G_z [−]	300			
Thermal diffusivity κ [m^2/s]	4.21E−07			
Flow unit	F6	F7	F8	F11
Average dimension of the flows				
Length [m]	14,915	8452	3176	5184
Flow width [m]	2386	1010	2094	2136
Channel width [m]	951	–	–	–
Thickness [m]	76	55	68	151
Slope (°)	4.1	4.6	2.7	1.8
Volume (area * thickness) [m^3]	2.2E + 09	5.7E + 08	5.4E + 08	1.8E + 09
Aspect ratio (A/H)[a]	98	65	46	26
Rheological parameters from the G_z approach				
Apparent viscosity from Jeffreys' equation [Pa s]	1E + 10	6E + 09	2E + 10	2E + 11
% error	32 %	35 %	39 %	40 %
Apparent viscosity from Hulme's model [Pa s]	6E + 08			
% error	27 %			
Yield strength [Pa]	1.4E + 05	1.1E + 05	8.2E + 04	1.2E + 05
% error	9 %	11 %	11 %	13 %
Yield strength from Hulme's model [Pa]	1.9E + 05			
% error	18 %			
Effusion rate [m^3/s]	60	20	12	9
% error	11 %	17 %	16 %	14 %
Velocity [m/day]	30	27	6	2
% error	15 %	19 %	14 %	18 %
t_{Gz} [days]	489	336	503	2271
% error	15 %	19 %	19 %	17 %
Kilburn and Lopes (1991) approach				
t_{KL} [days]	600	265	1318	2656
% error	25 %	24 %	28 %	28 %
Average				
Average duration [years]	1.5	0.8	2.5	6.7
Average effusion rate [m^3/s]	47	22	7	9
Average mass effusion rate [kg/s]	1.2E + 05	5.7E + 04	1.8E + 04	2.2E + 04

[a] According to Walker (1973), where A is the diameter of the corresponding circle of the flow area and H is the thickness of the flow

Alternatively, late lavas may have mixed with another, more radiogenic source depleted in trace elements that did not erupt from El Metate. The chemical data of Ownby et al. (2011) for volcanic rocks in the nearby Tancítaro area does not, however, include any composition with such low HREE values.

Source heterogeneities and crustal assimilation

The different isotopic compositions of early lavas (F1-F2-F4b) and late lavas (F5-F11-F12) indicate that they originated from a source affected by continental crust assimilation or from a heterogeneous mantle. More isotopic systems should be used to distinguish between these two hypotheses.

If crustal assimilation would be an important factor, its degree would need to be significant in order to explain the isotopic differences (Fig. 9c, d). Mineralogic evidence of strong contamination is essentially absent since only few Qz-xenocrysts were observed. These must have been picked up shortly before eruption.

Instead, the differences in isotopic and trace element compositions observed between the two lava groups and within the late lavas might have been caused by mantle heterogeneities. These could be derived from variable degrees of

enrichment in fluid-mobile elements (LIL: light REE, Rb, Cs, etc.) of the fluids expelled from slab-derived sediments and differences in the extent of depletion in immobile elements (heavy REE, high-field strength elements like Nb, Ta, Ti) by previous melting events as already postulated (e.g., Johnson et al. 2009 and references therein) for other volcanic rocks in the TMVB. The lower concentration of both mobile and immobile elements and the less radiogenic signature of the late lavas in comparison with the early lavas suggest that the former issued from a more depleted mantle source that was affected by lesser degrees of fluid enrichment. The cause of the abnormal Sr-rich composition of the most mafic late lavas (F5–F9) is not clear, but the near-MORB isotopic signature of these lavas excludes contamination by an old radiogenic Sr-rich crust. The high Sr/Y ratios of the late lavas may thus reflect a mantle source contaminated by Sr-rich fluid (or melt). Finally, the poorly fractionated HREE (of both lava groups) suggest that hornblende was a residue in the source, which has been interpreted by Ownby et al. (2011) to suggest an origin by partial melting of hornblende-rich gabbro-norite in the lower crust. However, Ortega-Gutiérrez et al. (2008) suggest that the lower crust in this area might consist of high-grade hydrous metamorphic rocks. Both cases seem discordant with the MORB-like isotopic composition of the late lavas, but more detailed geochemical studies are needed to better define the nature of the source.

Eruptive model

The more straightforward and simple model would consist of a first magma batch ascending continuously through the crust and erupting the early lava group followed by a second magma batch that then forms the late lavas. However, we prefer a model in which the magma that formed the late lavas stagnated in the crust before ascent and eruption of the early lava.

The magma batch that formed the late lavas (hornblende-bearing) required some residence time in the upper crust (~7–10 km depth) to allow for phenocryst growth. This would imply cooling and a concomitant viscosity increase, hindering further ascent and eruption. This could be overcome if a second, less viscous olivine-bearing batch passes by, suffering only minor cooling (limited stagnation upon ascent, see Fig. 10), and opens the path, erupting first. Accordingly, we propose a model that includes three main stages (Fig. 12):

Stage A. Some time prior to the eruption, a first voluminous batch with a heterogeneous, near-MORB isotopic signature, MgO-poor but Sr and H_2O-rich low-viscosity magma (10^2–10^3 Pa s) was emplaced in the upper crust at depths of ~7–10 km where it underwent mainly plagioclase and hornblende crystallization and fractionation.

Stage B. This was followed by the ascent of a second smaller magma batch that was isotopically more radiogenic, less differentiated (MgO richer) and hotter (>1100 °C). This batch likely bypassed the first batch before erupting at the surface and forming the early lava group (F1–F4b). The lack of chemical and textural evidence for mixing between the two magmas suggests little interaction between them. Although the exact sequence of flow emplacement is not

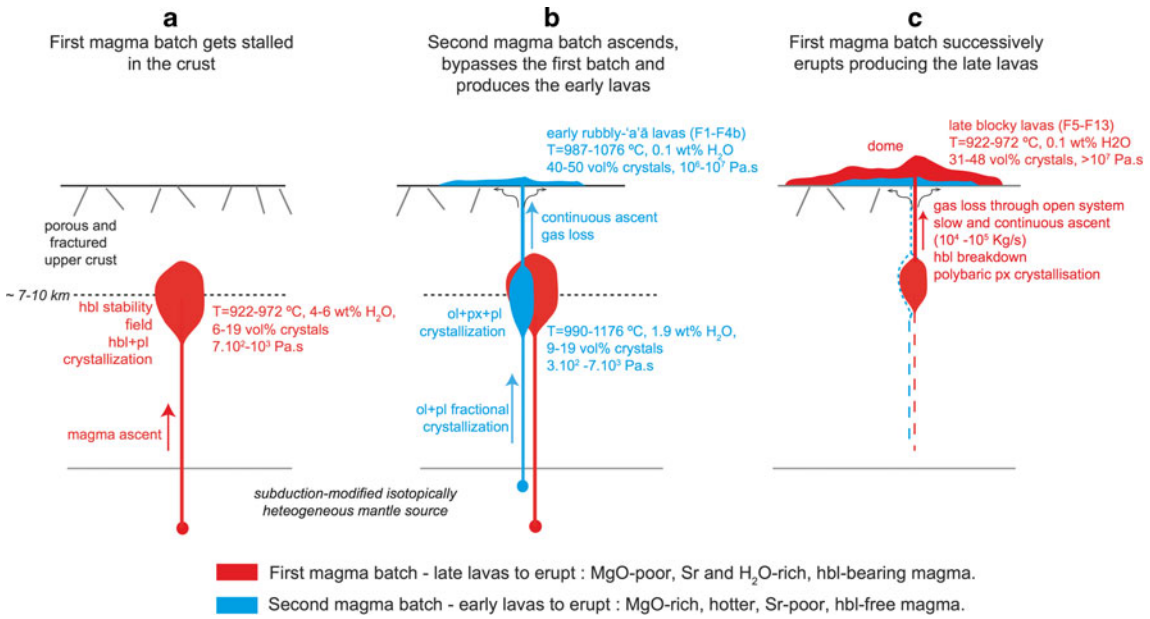

Fig. 12 Schematic model depicting magma ascent from the mantle, temporary storage in the upper crust, and eruptive sequence of early (*blue*) and late (*red*) lavas

known for early lavas, it seems more likely that the most mafic, olivine-bearing, hottest (~1076 °C), and less viscous lava (F1) was the first to erupt. The subsequent more evolved, olivine-free magma crystallized pyroxene at shallow levels (~10 km) and produced the more silicic early lavas (F2–F4) at lower temperatures (~990 °C). A small lava volume of intermediate composition, likely trapped in the complex plumbing network or resulting from another magma input, erupted subsequently out of F4 forming the small lava lobe F4b. All these early lavas have relatively low emplacement viscosities (10^6–10^7 Pa s) and form thin (<40 m) rubbly-'a'ā to blocky flows.

Stage C. Once the initial source exhausted and the vent opened, the first magma batch (from stage A, as described above) that stalled at depth followed on the heels in the same dike system to reach the surface producing the hornblende-bearing late lava group (F5–F13). This larger batch shows progressive enrichment in SiO_2, decreasing Sr contents, and increasingly radiogenic isotope compositions with time, possibly due to mixing with an unknown third component. This magma erupted entirely effusively at ~922–972 °C and lavas rapidly developed high viscosities (from 10^7 to 10^{11} Pa s) during emplacement to form thick (60–150 m) blocky lava flows. The flows that were emitted to the south (F6–F7) nevertheless reached long distances from the vent (<15 km) probably due to the combination of low heat loss during emplacement (efficient thermal insulation by the formation of a carapace) and a great volume emitted on a pronounced gradient.

Eruptive dynamics

If erupted explosively, the large magma volume involved in the El Metate eruption would have produced a major Plinian eruption (volcanic explosivity index >5) with a tremendous impact on surrounding populations (Chevrel et al. 2016). It is worth noting that all eruptions of large volumes of andesitic magma in the Holocene have been explosive (Table 3 in Chevrel et al. 2016), and hence, in this respect, El Metate's eruption is intriguing. For hazard assessment purposes, it is of fundamental importance to understand why magmas with similar compositions and physical properties can display contrasting eruption styles: Why did El Metate erupt effusively and not explosively? Magma viscosity is not the only parameter determining how volatiles degas from the magma (explosive vs. effusive style). Degassing processes also depend on whether closed vs. open system conditions become established in upper crustal levels prior to eruption (e.g., Cashman 2004). The effusive style of El Metate implies efficient open system degassing, through an open conduit and permeable walls, of a magma that ascended at rates that were sufficient to sustain the effusive activity throughout the eruption allowing continuous passive gas escape. In this context, the mass eruption rate was estimated for El Metate (assuming continuous and sustained activity) by multiplying the effusion rate (obtained by the morphological approach) for late lavas (5–50 m^3/s) by the density of typical andesitic lava with 0–30 % of vesicles (1820–2600 kg/m^3). This yielded a mass eruption rate in the range of 10^4–10^5 kg/s, a value that falls at the limit between the explosive and effusive eruption styles for a wide range of observed historic cases (Cashman 2004). This value is similar to the mass eruption rate reported for the initial violent Strombolian activity of Paricutin volcano (Pioli et al. 2008) but only slightly higher than the long-term effusion rates observed at lava lakes and domes (Pyle 2000).

The texture of hornblende crystals is strongly dependent on decompression rates because this affects the time available for the crystals to react to decreasing melt water contents (Rutherford and Hill 1993; Rutherford and Gardner 2000; Rutherford and Devine 2003). The rates calculated above correspond to the limit at which the minerals start to break down in the experiments of Rutherford and Hill (1993). This may explain why, in El Metate lavas, some crystals are still intact while others have partly to fully suffered breakdown and recrystallization. Alternatively, there may have been heterogeneities in the decompression rate experienced by the ascending magma due, for example, to velocity gradients across the conduit. Opacite rims around the crystals likely grew by oxidation and dehydrogenation during lava emplacement (Garcia and Jacobson 1979).

It is worth noting that El Metate's early lava type (MgO-rich andesite with abundant olivine) is frequent in the MGVF (e.g., Jorullo, Paricutin, etc., Hasenaka and Carmichael 1987), while the El Metate late lava type (hornblende-bearing MgO-poor andesite) occurs more rarely and commonly forms smaller edifices. Specific conditions must have existed at El Metate to allow for such a large volume of an initially hydrous, low-*T*, crystal-rich magma to reach the surface and erupt in a solely effusive manner. Intense passive degassing of the magma must have occurred prior to or during ascent to prevent explosive eruption. We envision a scenario in which the second magma batch that produced the early lavas (which were the hotter, more fluid, and also more frequent in the MGVF) opened the conduit allowing gas escape from the hornblende-bearing first magma batch (at that time still residing at depth) and therefore facilitating its final ascent by

reducing the pressure gradient. Brenna et al. (2010) proposed a similar scenario, according to which a low volume magma acted as a trigger or path-opener for the eruption of a shallower derived, larger volume magma and that the two magmas used the same single-dike plumbing system.

The above scenario leads to the question of why the hornblende-bearing first magma batch did not reach the surface first but instead became temporarily stalled at depth. On the basis of petrological experiments, Carmichael (2002) demonstrated that a decompressing andesitic hydrous (but relatively cold) magma, such as El Metate's first batch, that reaches hornblende stability at low pressures will crystallize readily, yielding to viscosity increase, and thus more likely become stalled during ascent, than a hotter and less hydrous magma (such as El Metate's second magma batch). The eruption of El Metate's late lavas thus exemplifies the specific conditions under which hornblende-bearing crystal-rich magmas can erupt. The above implies that, given the evidence for a hydrous mantle below the MGVF (Johnson et al. 2009), large volumes of this magma type may be stalled in the crust underneath the MGVF.

Lava emplacement and duration of the eruption

Active andesitic flows of the size of those emitted by El Metate have never been witnessed, which makes it difficult to make interpretations about their emplacement style. The viscosities derived from petrological parameters are first-order approximations because they do not take into account heterogeneities in crystal and bubble distribution, crystal-crystal interactions, strain-rate effects (Caricchi et al. 2007; Costa et al. 2009; Lavallée et al. 2007), or viscous heating (Cordonnier et al. 2012). Morphologically derived parameters are also subject to much uncertainty given that most of them assume simple, nonrealistic rheology (Newtonian). More complex formulations (e.g., Castruccio et al. 2010, 2014) require consideration of a large set of additional petrographic and morphometric parameters (fraction of the crystals formed after flow emplacement, parameterization of the yield strength and shear rate dependency as a function of crystal content, flow thickness during the eruption, etc.) that cannot be inferred for flows whose emplacement was not directly observed, and would require more complex modeling which is beyond the scope of this paper.

Nevertheless, the viscosities and effusion rates calculated here are quite comparable to those reported for smaller active blocky lava flows (e.g., Lonquimay, Chile; Naranjo et al. 1992; Santiaguito, Guatemala; Harris et al. 2004) but slightly higher than expected for andesitic flows (e.g., Kilburn 2000; Harris and Rowland 2015). The inferred yield strength values ($\sim 10^5$ Pa) are also similar to values obtained for intermediate to silicic lava flows and domes (Harris and Rowland 2015).

The effusion rates estimated here might be too high because their calculation considers a constant magma output rate, although the latter was observed to decrease over time in the few active flows that have been observed directly. For example, the effusion rates during the eruption of the andesitic lava flow from Lonquimay, Chile, started at 80 m^3/s and decreased rapidly to <10 m^3/s within the first 50 days, for a total duration of 330 days (Naranjo et al. 1992). Furthermore, well-isolated flows could continue advancing despite a decrease or cessation of the lava supply. An example for this is the rhyolitic lava flow from Cordón Caulle, Chile, which continued to advance as far as 3.6 km from the vent, although the lava supply had ceased 6–8 months earlier (Tuffen et al. 2013). Still today, it is not possible to anticipate with certainty how long the Cordón Caulle flow will remain active. In addition, the time that elapsed between the extrusion of each of El Metate's lava flows is unknown. However, given the young age (~AD 1250) of this volcano and in the absence of any reference to its activity in the early colonial chronicles, it is safe to assume that El Metate's lavas must have been essentially cold by the time of the arrival (AD 1520s) of the Spaniards in Michoacán. Accordingly, the maximum emplacement duration of the entire volcano must have been less than 275 years (Chevrel et al. 2016). On the other hand, assuming a continuous and successive (one after the other) eruption of all lava flows (representing ~10.8 km^3, non-DRE; Chevrel et al. 2016) at a rate of ~10 m^3/s, the formation of El Metate should have taken at least ~35 years.

Conclusions

Stratigraphic relations and lava flow morphological parameters together with viscosity estimates all indicate that the entire eruption of El Metate was purely effusive and continuous. At the end, 103 km^2 of terrain was covered by lava flows forming a monogenetic shield with a total volume of 9.2 km^3. Hence, El Metate was formed by the largest andesitic effusive eruption worldwide and the most voluminous eruption in Mexico during Holocene times, and it certainly had a significant impact on the environment and human populations (Chevrel et al. 2016).

Our detailed study of El Metate volcano, the youngest andesite shield of the MGVF, shows that its lava flows originated from two separate magma batches that had different mineralogical and chemical compositions, as well as distinct Sr-Nd-Pb isotope signatures. The source for both batches was a subduction-modified heterogeneous mantle. Mineral thermobarometry reveals that after initial ascent through the crust, the first batch became temporarily stalled at a depth of ~7–10 km, allowing for crystallization and fractionation. Then, the second batch ascended and evolved independently, bypassed the first batch without major mingling or mixing,

and erupted effusively to form the early lava flows (F1–F4). The first batch followed immediately after, along the same conduit and produced the late lava flows (F5–F13).

The continuous ascent rates must have been slow enough to allow extensive open system degassing (outgassing) of magma as it was rising to the surface, thereby preventing explosive eruption. Instead, effusive outpouring of a large volume of andesitic magma formed more than a dozen lava flows. Fed by a relatively high and sustained mass eruption rate (10^4–10^5 kg/s), some of the most voluminous (~2 km^3) lava flows reached distances of up to ~15 km from the vent, aided by the pre-existing slope and low heat loss during emplacement. The morphologies and compositions of early Mg-rich lavas indicate lower viscosities (10^6–10^7 Pa s), while the late hornblende-rich lavas (10^7 to 10^{11} Pa s) formed thicker viscous flows. Estimates of flow emplacement duration yielded ~2 years for the longest and ~7 years for the thickest flow, respectively. Successive emplacement of all flows probably took ~35 years.

Finally, El Metate is one of ~400 medium-sized volcanoes in the MGVF. Whether many of them followed a similar eruption pattern is unclear, however no other *Mexican shield* displays such a well-exposed morphology. Other previously studied Mexican shields such as Cerro Paracho or El Estribo are clearly composite and polygenetic (Pola et al. 2014; Siebe et al. 2014; Chevrel et al. 2016). Although El Metate represents an exceptional volume of lava, many other examples of similarly thick blocky andesite lava flows exist in the MGVF. Many of them are isolated and have a much smaller volume but may represent other examples for the effusive eruption of a similar magma type. Further studies of such voluminous blocky flows are needed to both better understand their mechanism of emplacement, as well as their role in the tectonic evolution and eruption dynamics of the MGVF.

Acknowledgments Field and laboratory costs were defrayed from projects funded by the Consejo Nacional de Ciencia y Tecnología (CONACyT-167231 and 152294) and the Dirección General de Asuntos del Personal Académico UNAM-DGAPA IN-101915 and 105615 granted to C. Siebe and M.-N. Guilbaud. M.O. Chevrel was funded by a UNAM-DGAPA postdoctoral fellowship (2014–2016). Peter Schaaf, Teodoro Hernández Treviño, Gabriela Solís-Pichardo, and Gerardo Arrieta supervised the isotopic analyses at LUGIS, and Carlos Linares López helped with the microprobe analyses at UNAM. We thank K. Putirka, F. Ridolfi, L. Waters, and R. Lange for allowing free access of Excel spreadsheets used for thermobarometry calculations and Fraser Goff for constructive discussion and comments on the manuscript. Sergio Salinas and Juan Ramón de la Fuente (UNAM) and Nicolás Vidales and his family from the Purépecha town of Turícuaro were helpful during fieldwork. We thank Hannah Dietterich, Dawnika Blatter, and an anonymous reviewer for their constructive comments and valuable suggestions as well as Paul Wallace for his comments and editorial handling of the manuscript.

References

Ban M, Hasenaka T, Delgado-Granados H, Takaoka N (1992) K-Ar ages of lavas from shield volcanoes in the Michoacán-Guanajuato volcanic field, México. Geofis Int 31(4):467–473

Baptista AR, Mangold N, Ansan V, Baratoux D, Masson P, Lognonné P, Williams D, Bleacher JE, Neukum G (2008) A swarm of small shield volcanoes on Syria Planum, Mars. J Geophys Res 113: E09010

Beattie P (1993) Olivine-melt and orthopyroxene-melt equilibria. Contrib Mineral Petrol 115:103–111

Blatter DL, Hammersley L (2010) Impact of the Orozco Fracture Zone on the central Mexican Volcanic Belt. J Volcanol Geoth Res 197:67–84

Brenna M, Cronin SJ, Smith IEM, Kwan Sohn Y, Németh K (2010) Mechanisms driving polymagmatic activity at a monogenetic volcano, Udo, Jeju Island, South Korea. Contrib Mineral Petrol 160:931–950

Brey GP, Köhler T (1990) Geothermobarometry in four-phase lherzolites II. New thermobarometers, and practical assessment of existing thermobarometers. J Petrol 31:1353–1378

Caricchi L, Burlini L, Ulmer P, Gerya T, Vassalli M, Papale P (2007) Non-Newtonian rheology of crystal-bearing magmas and implications for magma ascent dynamics. Earth Planet Sci Lett 264:402–419

Carmichael ISE (2002) The andesite aqueduct: perspectives on the evolution of intermediate magmatism in west-central (105–99°W) Mexico. Contrib Mineral Petrol 143:641–663

Cashman KV (2004) Volatile controls on magma ascent and eruption. In: Sparks RSJ, Hawkesworth CJ (eds) The state of the planet: frontiers and challenges in geophysics. Geophysical Monograph 150 Washington DC, Am Geophys Union

Castruccio A, Rust AC, Sparks RSJ (2010) Rheology and flow of crystal-bearing lavas: insights from analogue gravity currents. Earth Planet Sci Lett 297:471–480

Castruccio A, Rust AC, Sparks RSJ (2013) Evolution of crust- and core-dominated lava flows using scaling analysis. Bull Volcanol 75:681

Castruccio A, Rust AC, Sparks RSJ (2014) Assessing lava flow evolution from post-eruption field data using Herschel–Bulkley rheology. J Volcanol Geoth Res 275:71–84

Chevrel MO, Platz T, Hauber E, Baratoux D, Lavallée Y, Dingwell DB (2013) Lava flow rheology: a comparison of morphological and petrological methods. Earth Planet Sci Lett 384:109–120

Chevrel MO, Siebe C, Guilbaud M-N, Salinas S (2016) The AD 1250 El Metate shield volcano (Michoacán): Mexico's most voluminous Holocene eruption and its significance for archeology and hazards. The Holocene 26(3):471–488

Cioni R, Funedda A (2005) Structural geology of crystal-rich, silicic flows: a case study from San Pietro Island (Sardinia, Italy). Geol Soc Am Spec Paper 396:1–14

Class C, Lehnert K (2012) PetDB expert MORB (mid-ocean ridge basalt) compilation. EarthChem Library. http://dx.doi.org/10.1594/IEDA/100060

Connor CB (1987) Structure of the Michoacán-Guanajuato volcanic field, Mexico. J Volcanol Geoth Res 33:193–200

Connor CB (1990) Cinder cone clustering in the Trans-Mexican Volcanic Belt: implications for structural and petrologic models. J Geophys Res 92(B12):19395–19405

Cordonnier B, Schmalholz SM, Hess K-U, Dingwell DB (2012) Viscous heating in silicate melts: an experimental and numerical comparison. J Geophys Res 117:B02203

Costa A, Caricchi L, Bagdassarov N (2009) A model for the rheology of particle-bearing suspensions and partially molten rocks. Geochem Geophys Geosyst 10:1525–2027

Decker RW, Wright TL, Stauffer PH (1987) Volcanism in Hawaii. US Geol Surv Prof Paper. 1350p

de Silva SL, Self S, Francis PW, Drake RE, Carlos RR (1994) Effusive silicic volcanism in the Central Andes: the Chao dacite and other young lavas of the Altiplano-Puna Volcanic Complex. J Geophys Res 99(B9):17805–17825

Eichelberger JC (1975) Origin of andesite and dacite: evidence of mixing at Glass Mountain in California and at other circum-Pacific volcanoes. Geol Soc Am Bull 86:1381–1391

Francis PW, Roobol MJ, Walker GPL, Cobbold PR, Coward M (1974) The San Pedro and San Pablo volcanoes of northern Chile and their hot avalanche deposits. Geol Rundsch 63:357–388

Fries C (1953) Volumes and weights of pyroclastic material, lava and water erupted by Paricutin Volcano, Michoacan, Mexico. Trans Am Geophys Union 34:603–616

Garcia MO, Jacobson SS (1979) Crystal clots, amphibole fractionation, and the evolution of calc-alkaline magmas. Contrib Mineral Petrol 69:319–327

Giordano D, Russell JK, Dingwell DB (2008) Viscosity of magmatic liquids: a model. Earth Planet Sc Lett 271:123–134

Gómez-Tuena A, Orozco-Esquivel MT, Ferrari L (2007) Igneous petrogenesis of the Trans-Mexican Volcanic Belt. In: Alaniz-Álvarez SA, Nieto-Samaniego AF (eds) Geology of México: celebrating the centenary of the Geological Society of México, vol 422, Geol Soc Am Spec Pap., pp 129–181

González Díaz E (1972) Descripción geológica de la Hoja 30d, Payun Matru. Direc Gen Min Geol Hidrol, Bol 130, 92p

Greeley R (1982) The Snake River Plain, Idaho: representative of a new category of volcanism. J Geophys Res 87(B4):2705–2712

Guest JE, Sanchez J (1969) A large dacitic lava flow in northern Chile. Bull Volcanol 33:778–790

Guest JE, Murray JB (1976) Volcanic features of the nearside equatorial lunar maria. J Geol Soc 132:251–258

Guest JE, Bulmer MH, Aubele J, Beratan K, Greeley R, Head JW, Michaels G, Weitz C, Wiles C (1992) Small volcanic edifices and volcanism in the plains of Venus. J Geophys Res 97(E10):15,949–15,966

Guilbaud M-N, Siebe C, Salinas S (2009) Excursions to Paricutin and Jorullo (Michoacán), the youngest volcanoes of the Trans-Mexican Volcanic Belt. A commemorative fieldtrip on the occasion of the 250th anniversary of Volcán Jorullo's birthday on September 29, 1759. Impretei S.A., México, D.F

Guilbaud M-N, Siebe C, Layer P, Salinas S, Castro-Govea R, Garduño-Monroy VH, Le Corvec N (2011) Geology, geochronology, and tectonic setting of the Jorullo Volcano region, Michoacán, México. J Volcanol Geoth Res 201:97–112

Guilbaud M-N, Siebe C, Layer P, Salinas S (2012) Reconstruction of the volcanic history of the Tacámbaro-Puruarán area (Michoacán, México) reveals high frequency of Holocene monogenetic eruptions. Bull Volcanol 74:1187–1211

Griffiths RW, Fink JH (1993) Effects of surface cooling on the spreading of lava flows and domes. J Fluid Mech 252:661–102

Harris AJL, Flynn LP, Matias O, Rose WI, Cornejo J (2004) The evolution of an active silicic lava flow field: an ETM+ perspective. J Volcanol Geoth Res 135:147–168

Harris AJL, Rowland SK (2015) Lava flows and rheology. In: Sigurdsson H, Houghton BF, McNutt SR, Rymer H, Stix J (eds) Encyclopedia of volcanoes, 2nd edn. Academic, London

Hasenaka T (1994) Size, distribution and magma output rates for shield volcanoes of the Michoacán-Guanajuato volcanic field, Central Mexico. J Volcanol Geoth Res 63:13–31

Hasenaka T, Ban M, Delgado-Granados H (1994) Contrasting volcanism in the Michoacán-Guanajuato volcanic field, central Mexico: shield volcanoes vs. cinder cones. Geofis Int 33(1):125–138

Hasenaka T, Carmichael ISE (1985a) Compilation of location, size, and geomorphological parameters of volcanoes of the Michoacán-Guanajuato volcanic field, central Mexico. Geofis Int 24(4):577–607

Hasenaka T, Carmichael ISE (1985b) The cinder cones of Michoacán-Guanajuato, central Mexico: their age, volume and distribution, and magma discharge rate. J Volcanol Geoth Res 25:105–124

Hasenaka T, Carmichael ISE (1986) Metate and other shield volcanoes of the Michoacán-Guanajuato. Mexico Trans Am Geophys Union 67: 44

Hasenaka T, Carmichael ISE (1987) The cinder cones of Michoacán-Guanajuato, central Mexico: petrology and chemistry. J Petrol 28: 241–269

Herrmann W, Berry RF (2002) MINSQ—a least square spreadsheet method for calculating mineral proportions from whole rock major element analyses. Geochem Explor Environ, Anal 2:361–368

Hildreth W (2007) Quaternary magmatism in the Cascades—geologic perspectives. USGS Professional Paper 1744. U.S. Geological Survey, Reston, Virginia, 125p.

Hulme G (1974) The interpretation of lava flow morphology. Geophys J Roy Astr Soc 39:361–383

Hulme G, Fielder G (1977) Effusion rates and rheology of lunar lavas. Philos Trans R Soc Lond S-A 285:227–234

Jeffreys H (1925) The flow of water in an inclined channel of rectangular section. Philosophical Magazine Series 6, 49(293): 793–807

Johnson ER, Wallace PJ, Granados HD, Manea VC, Kent AJ, Bindeman IN, Donegan CS (2009) Subduction-related volatile recycling and magma generation beneath central Mexico: insights from melt inclusions, oxygen isotopes and geodynamic models. J Petrol 50(9): 1729–1764

Kerr RC, Griffiths RW, Cashman KV (2006) Formation of channelized lava flows on an unconfined slope. J Geophys Res 111:B10206

Kilburn CRJ (2000) Lava flows and flow fields. In: Sigurdsson H, Houghton BF, McNutt SR, Rymer H, Stix J (eds) Encyclopedia of volcanoes. Academic, London

Kilburn CRJ, Lopes R (1991) General patterns of flow field growth: Aa and blocky lavas. J Geophys Res 96(B12):19,721–19,732

Kim Y, Miller MS, Pearce F, Clayton RW (2012) Seismic imaging of the Cocos plate subduction zone system in central Mexico. Geochem Geophys Geosy 13(7):Q07001

Krieger IM, Dougherty TJ (1959) A mechanism for non-Newtonian flow in suspensions of rigid spheres. J Rheol 3:137–152

Laubier M, Grove TL, Langmuir CH (2014) Trace element mineral/melt partitioning for basaltic and basaltic andesitic melts: an experimental and laser ICP-MS study with application to the oxidation state of mantle source regions. Earth Planet Sci Lett 392:265–278

Lavallée Y, Hess K-U, Cordonnier B, Dingwell DB (2007) Non-Newtonian rheological law for highly crystalline dome lavas. Geology 35:843–846

LeBas MJ, Lemaitre RW, Streckeisen A, Zanettin B (1986) A chemical classification of volcanic rocks based on the total alkali silica diagram. J Petrol 27(3):745–750

Lefler E (2011) Genauigkeitsbetrachtung bei der Ermittlung rheologischer Parameter von Lavaströmen aus Fernerkundungsdaten. Freie Universität Berlin, Berlin, B.Sc. thesis, 75p

Losantos E, Cebriá JM, Morán-Zenteno DJ, Martiny BM, López-Ruiz J (2014) Condiciones de cristalización y diferenciación de las lavas del volcán El Metate (Campo Volcánico de Michoacán-Guanajuato, México). Estud Geol-Madrid 70(2):e020

Manga M, Castro J, Cashman KV, Loewenberg M (1998) Rheology of bubble-bearing magmas. J Volcanol Geoth Res 87:15–28

McDonough WF, Sun SS, Ringwood AE, Jagoutz E, Hofmann AW (1992) Potassium, rubidium, and cesium in the earth and moon and the evolution of the Earth's mantle. Geochim Cosmochim Acta 56(3):1001–1012

Mueller S, Llewellin EW, Mader HM (2010) The rheology of suspensions of solid particles. Trans R Soc Lond S-A 466:1201–1228

Naranjo JA, Sparks RSJ, Stasiuk MV, Moreno H, Ablay GJ (1992) Morphological, structural and textural variations in the 1988–1990

andesite lava of Lonquimay Volcano, Chile. Geol Mag 129(6):657–678

Nichols RL (1939) Viscosity of lava. J Geol 47:290–302

Ortega-Gutiérrez F, Elías-Herrera M, Dávalos-Elizondo MG (2008) On the nature and role of the lower crust in the volcanic front of the Trans-Mexican Volcanic Belt and its fore-arc region, southern and central Mexico. Revista Mexicana de Ciencias Geológicas 25(2): 346–364

Ownby SE, Delgado-Granados H, Lange RA, Hall CM (2007) Volcán Tancítaro, Michoacán, México. $^{40}Ar/^{39}Ar$ constraints on its history of sector collapse. J Volcanol Geoth Res 161:1–14

Ownby SE, Lange RA, Hall CM, Delgado-Granados H (2011) Origin of andesite in the deep crust and eruption rates in the Tancítaro-Nueva Italia region of the central Mexican arc. Geol Soc Amer Bull 123(1–2):274–294

Pardo M, Suárez G (1995) Shape of the subducted Rivera and Cocos plates in southern Mexico: seismic and tectonic implications. J Geophys Res 100(B7):12,357–12,373

Pinkerton H, Sparks RSJ (1976) The 1975 sub-terminal lavas, Mount Etna: a case history of the formation of a compound lava field. J Volcanol Geoth Res 1:167–182

Pinkerton H, Wilson L (1994) Factors controlling the lengths of channel-fed lava flows. J Volcanol Geoth Res 56:108–120

Pioli L, Erlund E, Johnson ER, Cashman KV, Wallace PJ, Rosi M, Delgado H (2008) Explosive dynamics of violent Strombolian eruptions: the eruption of Paricutin Volcano 1943–1952 (Mexico). Earth Planet Sci Lett 271:359–368

Pola A, Macías JL, Garduño-Monroy VH, Osorio-Ocampo S, Cardona-Melchor S (2014) Successive collapses of the El Estribo volcanic complex in the Pátzcuaro Lake, Michoacán, Mexico. J Volcanol Geoth Res 289:41–50

Prowatke S, Klemme S (2006) Trace element partitioning between apatite and silicate melts. Geochim Cosmochim Acta 70(17):4513–4527

Putirka KD (2008) Thermometers and barometers for volcanic systems. Rev Mineral Geochem 69:61–120

Pyle DM (2000) Sizes of volcanic eruptions. In: Sigurdsson H, Houghton BF, McNutt SR, Rymer H, Stix J (eds) Encyclopedia of volcanoes. Academic, London

Ridolfi F, Renzulli A, Pueriniet M (2010) Stability and chemical equilibrium of amphibole in calc-alkaline magmas: an overview, new thermobarometric formulations and application to subduction-related volcanoes. Contrib Mineral Petrol 160:45–66

Roggensack K (1992) Petrology and geochemistry of shield volcanoes in the central Mexican Volcanic Belt. PhD thesis. Dartmouth College, NH, USA, 173p

Rossi MJ (1996) Morphology and mechanism of eruption of postglacial shield volcanoes in Iceland. Bull Volcanol 57:530–540

Rust AC, Manga M (2002) Effects of bubble deformation on the viscosity of dilute suspensions. J Non-Newtonian Fluid Mech 104:53–63

Rutherford MJ, Devine JD (2003) Magmatic conditions and magma ascent rate as indicated by hornblende phase equilibria and reaction in the 1995–2002 Soufrière Hills magma. J Petrol 44:1433–1454

Rutherford MJ, Gardner JE (2000) Rate of magma ascent. In: Sigurdsson H, Houghton BF, McNutt SR, Rymer H, Stix J (eds) Encyclopedia of volcanoes. Academic, London

Rutherford MJ, Hill PM (1993) Magma ascent rates from amphibole breakdown: experiments and the 1980–1986 Mount St. Helens eruptions. J Geophys Res 98:19,667–19,685

Schaaf P, Stimac J, Siebe C, Macías JL (2005) Geochemical evidence for mantle origin and crustal processes in volcanic rocks from Popocatépetl and surrounding monogenetic volcanoes, central Mexico. J Petrol 46:1243–1282

Siebe C, Guilbaud M-N, Salinas S, Kshirsagar P, Chevrel MO, de la Fuente JR, Hernández-Jiménez A, Godínez L (2014) Monogenetic volcanism of the Michoacán-Guanajuato Volcanic Field: Maar craters of the Zacapu basin and domes, shields, and scoria cones of the Tarascan highlands (Paracho-Paricutin region). Fieldguide, pre-meeting fieldtrip (Nov. 13–17) for the 5th International Maar Conference (5IMC-IAVCEI), Querétaro, México

Sieron K, Siebe C (2008) Revised stratigraphy and eruption rates of Ceboruco stratovolcano and surrounding monogenetic vents (Nayarit, Mexico) from historical documents and new radiocarbon dates. J Volcanol Geoth Res 176:241–264

Sisson TW (1994) Hornblende-melt trace-element partitioning measured by ion microprobe. Chem Geol 117(1):331–344

Sun SS, McDonough WF (1989) Chemical and isotopic systematics of oceanic basalts: implications for mantle composition and processes. In: Saunders AD, Norry MJ (eds) Magmatism in the ocean basins, vol 42, Geological Society Special Publication., pp 313–345

Tepley FJ III, Lundstrom CC, McDonough WF, Thompson A (2010) Trace element partitioning between high-An plagioclase and basaltic to basaltic andesite melt at 1 atmosphere pressure. Lithos 118:82–94

Tiepolo M, Oberti R, Zanetti A, Vannuci R, Foley S (2007) Trace-element partitioning between amphibole and silicate melt. Rev Mineral Geochem 67:417–425

Tuffen H, James MR, Castro JM, Schipper CI (2013) Exceptional mobility of an advancing rhyolitic obsidian flow at Cordón Caulle volcano in Chile. Nature Communication 4:2709

Valentine GA, Connor CB (2015) Basaltic volcanic fields. In: Sigurdsson H, Houghton BF, McNutt SR, Rymer H, Stix J (eds) Encyclopedia of volcanoes, 2nd edn. Academic, London, pp 423–439

Verma SP (2000) Geochemistry of the subducting Cocos plate and the origin of subduction-unrelated mafic volcanic at the volcanic front of the central Mexican Volcanic Belt. In: Delgado H, Aguirre-Díaz G, Stock JM (eds) Cenozoic tectonics and volcanism of Mexico, vol 334, Geol Soc Am Spec Paper, pp 195–222

Wadge G, Lopes RMC (1991) The lobes of lava flows on Earth and Olympus Mons, Mars. Bull Volcanol 54:10–24

Walker GPL (1973) Lengths of lava flows. Philos Trans R Soc Lond 274: 107–118

Waters LE, Lange RA (2015) An updated calibration of the plagioclase-liquid hygrometer-thermometer applicable to basalts through rhyolites. Am Min 100:2172–2184

Whitford-Stark JL (1975) Shield volcanoes. In: Fielder G, Wilson L (eds) Volcanoes of the Earth, Moon and Mars. St. Martins, New York

Williams H (1950) Volcanoes of the Paricutin region, México: geologic investigations in the Paricutin area, México. US Geol Surv Bull 965-B:165–279

Wilson L, Head JW (1983) A comparison of volcanic eruption processes on Earth, Moon, Mars, Io and Venus. Nature 302:663–669